Charge Induced Disorder Controls the Thermal Conductivity of Entropy Stabilized Oxides

Jeffrey L. Braun,[1] Christina M. Rost,[1] Mina Lim,[2] Ashutosh Giri,[1] David H. Olson,[1] George Kotsonis,[2] Gheorghe Stan,[3] Donald W. Brenner,[2] Jon-Paul Maria,[2] and Patrick E. Hopkins[1,4,5,*]

[1]*Department of Mechanical and Aerospace Engineering,*
University of Virginia, Charlottesville, Virginia 22904, USA
[2]*Department of Materials Science and Engineering,*
North Carolina State University, Raleigh, North Carolina 27695, USA
[3]*Material Measurement Laboratory, National Institute of*
Standards and Technology, Gaithersburg, MD 20899, USA
[4]*Department of Materials Science and Engineering,*
University of Virginia, Charlottesville, Virginia 22904, USA
[5]*Department of Physics, University of Virginia, Charlottesville, Virginia 22904, USA*

(Dated: September 6, 2018)

Abstract

Manipulating a crystalline material's configurational entropy though the introduction of unique atomic species can produce novel materials with desirable mechanical and electrical properties. From a thermal transport perspective, large differences between elemental properties such as mass and interatomic force can reduce the rate at which phonons carry heat and thus reduce the thermal conductivity. Recent advances in materials synthesis have enabled the fabrication of entropy-stabilized ceramics, opening the door for understanding the implications of extreme disorder on thermal transport. Measuring the structural, mechanical, and thermal properties of single-crystal entropy stabilized oxides, we show that local ionic charge disorder can effectively reduce thermal conductivity without compromising mechanical stiffness. These materials demonstrate similar thermal conductivities to their amorphous counterparts, in agreement with the theoretical minimum limit, resulting in this class of material possessing the highest ratio of elastic modulus to thermal conductivity of any isotropic crystal.

---

[*] phopkins@virginia.edu

High entropy alloys (HEAs), consisting of five or more approximately equimolar compositions of elements,[1, 2] have proven to exhibit unique physical properties such as high hardness,[3] thermal stability,[4] structural stability,[5] as well as corrosion, oxidation, and wear resistance.[6–8] While microstructure and mechanical properties have been extensively studied, thermal properties, such as heat capacity and thermal conductivity, have been given far less attention.[9–11] Although the random distribution of atomic configurations in HEAs are appealing for understanding the role of configurational disorder on thermal transport, insight is limited by the significant electronic contribution that arises from the metallic nature of most HEAs, which can obscure insight into the lattice thermal conductivity. When nonmetal constituents comprise a disordered solid solution, the dynamics of thermal transport becomes dominated by phonons. However, only recently was the concept of entropy stabilization realized in ceramics,[12] allowing for an ideal platform to study the role of mass and interatomic force disorder beyond what has been previously accessible. Since the conception of these ceramics, high entropy oxides have demonstrated the capability for superionic mobility[13] and thermochemical water splitting.[14] Furthermore, high configurational entropy can be highly beneficial to the development of thermoelectric properties.[15] Understanding the general implications of extreme configurational entropy on the lattice thermal conductivity would greatly benefit the design of high entropy materials for use in such applications.

To this end, we study the thermal properties of a new class of mixed oxides analogous to their HEA metallic counterparts, entropy stabilized oxides (ESOs), characterized by their high configurational entropy that leads to structural and chemical stabilization through a local minimization of Gibbs free energy.[12] Each ESO forms a single phase, single crystal rocksalt structure having a fixed oxygen anion sublattice; between each oxygen atom pair sits a cation randomly selected among the equiprobable distribution of 5 or 6 unique elements. The ESOs (see Table I) include J14 ($Mg_xNi_xCu_xCo_xZn_xO$, $x = 0.2$), and five 6-cation oxides made up of the J14 composition plus an additional cation to include Sc (J30), Sb (J31), Sn (J34), Cr (J35), and Ge (J36). We show that ESOs possess amorphous-like thermal conductivities that, in contrast to analytical theory, drop by a factor of two when adding an additional cation species to a 5-cation crystal, regardless of the mass added. Using extended X-ray absorption fine structure, we isolate the mechanism of this reduction to atomic level disorder resulting from charge differences among the ions. This local atomic disorder manifests itself in an observable distortion of the oxygen sublattice while preserving long range crystallographic order measured with X-ray diffraction. This finding is further corroborated by molecular dynamics simulations that account for differences among interatomic
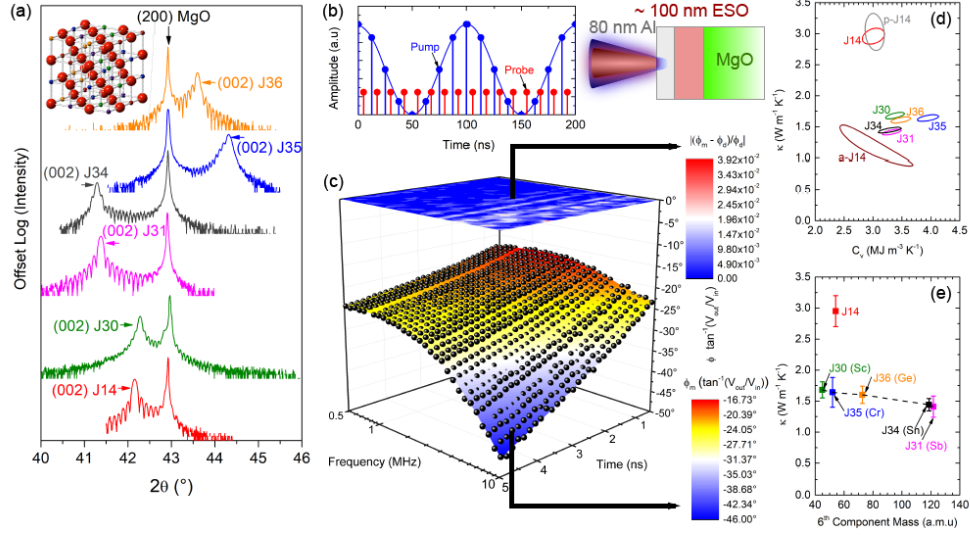
FIG. 1. Structural and Thermal Characterization. (a) 2θ-ω X-ray diffraction scan around the (200) MgO substrate peak. Inset shows J14 crystal structure with red anions representing oxygen and cation cites occupied by a random distribution of five distinct elements. (b) Schematic for TDTR/FDTR experiment: sample is 80 nm Aluminum on a ~100 nm ESO film grown on an MgO substrate. Laser heating by a modulated pulsed pump is detected by a probe by locking into the pump modulation frequency; the modulation frequency is varied and the probe is delayed in time relative to the pump, creating a time and frequency space to which to fit a thermal model. (c) Combined TDTR/FDTR experimental phase data ($\phi = \tan^{-1}(V_{\text{out}}/V_{\text{in}})$) and surface fit for J14 at room temperature (symbols), together with the best-fit thermal model and resulting normalized residuals ($|(\phi_{\text{m}} - \phi_{\text{d}})/\phi_{\text{d}}|$). (d) Contour of deviation sum as functions of κ and C_{v} all thin film samples, as determined by the 95% confidence interval in the normalized residuals. Sample compositions are provided in Table I. (e) κ vs. 6th-cation atomic mass for 6-cation ESOs. For reference, κ of J14 is also shown at it's average cation mass.

forces through electrostatic interactions based on Bader charges taken from density functional theory calculations.

ESO thin films were grown epitaxially on MgO substrates using pulsed laser deposition. Because the ESOs are pinned in-plane to the MgO substrate, their in-plane lattice parameters match that of MgO at 4.21 Å, whereas the out-of-plane lattice parameters vary slightly based on com-

Name	Composition	d (nm)	$\kappa \left(\frac{\text{W}}{\text{mK}}\right)$	$C_v \left(\frac{\text{MJ}}{\text{m}^3\text{K}}\right)$	E (GPa)
J14	$Mg_xNi_xCu_xCo_xZn_xO$, $x = 0.2$	114 ± 2	2.95 ± 0.25	3.01 ± 0.49	152.0 ± 10.6
J30	$Mg_xNi_xCu_xCo_xZn_xSc_xO$, $x = 0.167$	149 ± 4	1.68 ± 0.13	3.37 ± 0.42	236.7 ± 15.9
J31	$Mg_xNi_xCu_xCo_xZn_xSb_xO$, $x = 0.167$	117 ± 6	1.41 ± 0.17	3.29 ± 0.54	158.4 ± 10.9
J34	$Mg_xNi_xCu_xCo_xZn_xSn_xO$, $x = 0.167$	118 ± 2	1.44 ± 0.10	3.29 ± 0.44	180.8 ± 17.9
J35	$Mg_xNi_xCu_xCo_xZn_xCr_xO$, $x = 0.167$	109 ± 8	1.64 ± 0.24	3.96 ± 0.75	151.0 ± 9.2
J36	$Mg_xNi_xCu_xCo_xZn_xGe_xO$, $x = 0.167$	109 ± 3	1.60 ± 0.14	3.55 ± 0.48	229.9 ± 21.2

TABLE I. Thermal and physical properties of ESOs at room temperature. Compositions and measured properties include film thickness (d), thermal conductivity (κ), volumetric heat capacity (C_v), and elastic modulus (E).

position. Crystal structures were characterized using X-ray diffraction (XRD). Figure 1(a) shows the 2θ-ω XRD scan around the (200) MgO substrate peak. Lower (higher) 2θ indicates larger (smaller) out of-plane lattice parameters. Thermal characterization was performed using a combined time- and frequency-domain thermoreflectance technique (see Methods) to simultaneously measure the thermal conductivity (κ) and volumetric heat capacity (C_v) of the thin-film ESO samples by modulating the pump heating event over a range of frequencies large enough to decouple thermal diffusivity from thermal effusivity. A schematic of the experiment and the sample geometry is shown in Fig. 1(b). The resulting best-fit surface model and data are shown in Fig. 1(c) for J14, along with the normalized residuals, for the phase as a function of delay time and modulation frequency. From this, we follow the procedure outlined by Wang et al.[16] to determine the 95% confidence interval of fitted thermal conductivity and heat capacity based on the 2 standard deviation difference from the minimum normalized residual. Figure 1(d) shows the results for J14 and all 6-component ESOs, where contour lines indicate the combinations of κ and C_v corresponding to a 95% confidence interval.

There is a strong reduction in thermal conductivity between J14 and all 6-cation oxides; variation in κ among the latter are within 20% of one another and follow an expected decreasing trend with heavier average cation mass, as shown in Fig. 1(e). Accounting for uncertainties arising from film thicknesses and thermal properties does not explain this reduction from 5- to 6-cations. This finding suggests that there is an enhanced level of phonon scattering intrinsic to the 6-cation oxides compared to J14 that is dictating the observed reduction in thermal conductivity. Further-

more, a 105 nm polycrystalline J14 sample (p-J14) was fabricated on an amorphous SiO_2 (a-SiO_2) substrate; grain sizes were on the order of 50-100 nm as determined by atomic force microscopy (AFM). Grain boundaries typically scatter phonons on the order of the grain size,[17, 18] which would reduce the thermal conductivity of p-J14 relative to single crystal J14. Because the substrate is a-SiO_2 in this case, heat capacity and thermal conductivity cannot be decoupled (see Supporting Information for details). However, if we assume that the heat capacity is that of J14, the thermal conductivity is, within uncertainty, equal to that of J14. This indicates that phonon scattering at grain boundaries negligibly affects the thermal conductivity, suggesting that the phonons contributing most strongly to thermal transport in J14 have mean free paths smaller than this average grain size. Moreover, this result indicates that even with additional external scattering mechanisms, the thermal conductivity of J14 does not reduce to those of the 6-cation oxides. To understand the significance of this reduction in thermal conductivity, we measure a 78 nm amorphous J14 (a-J14) film grown on a-SiO_2. Again assuming the same heat capacity as J14, the thermal conductivity of a-J14 is 1.16 ± 0.16, almost a third of that of J14, and within 20% of the thermal conductivity of J31. This amorphous thermal conductivity is typically assumed to be the minimum limit to the intrinsic thermal conductivity of a solid.[19]

Reduced crystalline thermal conductivity approaching the amorphous limit is an attractive property to several applications, including thermoelectric power generation[20] and thermal barrier coatings,[21] where crystalline materials allow for the desirable electronic properties and temperature stability necessary for extreme environments. Such reduction is often achieved via nanostructuring with defects and/or interfaces, the latter of which resulted in the lowest thermal conductivity measured in a fully dense solid at 0.05 W m^{-1} K^{-1} for WSe_2 in the cross-plane direction,[22] a $30\times$ reduction over the c-axis thermal conductivity of single-crystal WSe_2. For macroscale applications in which films inevitably become large enough that grains of varying orientations form, thermal conductivity reduction in one crystallographic direction does not have significant benefit. Thus, for isotropic crystals, such reduction is typically achieved via increasing compositional disorder,[23] which can lead to mass mismatch, atomic radii mismatch, and local atomic strain that results in additional phonon scattering. For example, mixed crystals with controlled disorder were shown to have thermal conductivities that approach their minimum limit.[19] Similarly, unary and binary compound superatomic crystals were shown to have amorphous-like thermal conductivities when orientational disorder is present.[24] On the other hand, many complex crystals such as the cubic I-V-VI_2 semiconductor $AgSbTe_2$ have intrinsically glass-like thermal conductivities[25]

FIG. 2. Thermal and elastic properties of crystals. (a) Thermal conductivity (κ) vs. elastic modulus (E) for a wide range of isotropic crystals at room temperature. Materials are grouped into metals (squares) and nonmetals (triangles), the former having the subset of high entropy alloys (open squares) and the latter having the subset of ESOs (circles). (b) Ratio of E to κ for the highest-ratio crystals from (a). A table of data and references can be found in the Supporting Information.

attributed to extreme nanoscale domains with different orderings on the cation sublattice.[26]

Regardless of the mechanism, a thermal conductivity reduction generally comes at the expense of a crystal's stiffness, as determined by its elastic modulus. This is shown in Fig. 2(a), where thermal conductivity is plotted as a function of elastic modulus for a wide array of isotropic crystals. Whereas metals can maintain a relatively high thermal conductivity due to contribution from electron transport, phonons are the dominant heat carriers in nonmetals; reduction of elastic modulus is indicative of a reduction in phonon group velocity and energies, resulting in a lowered thermal conductivity. As shown in Fig. 2(a), the regime of simultaneously stiff and insulative

crystals is unpopulated, despite the need in practical applications such as thermal barrier coatings. We show that ESOs, whose elastic modulus is measured with contact resonance atomic force microscopy (CR-AFM), represent a step towards filling this void. In fact, in Fig. 2(b) we quantify the ratio of elastic modulus to thermal conductivity (E/κ) to show that ESOs fall in line with the highest E/κ crystals at room temperature, surpassing prominent thermal barrier coating materials such as zirconates $BaZrO_3$, and $La_2Zr_2O_7$ and the most commonly used Y_2O_3-stabilized ZrO_2 (YSZ).[27] By comparison, HEAs have elastic moduli falling anywhere from 20 to 180 GPa,[28] while thermal conductivities generally fall in the range of >10 W m^{-1} K^{-1},[28] The general metallic nature of most HEAs mean that they will have relatively large contributions from electrons to thermal conductivity. However, recent developments in HEAs for use in thermoelectric applications[11, 29], have demonstrated that HEAs can have thermal conductivities as low as 0.5 W m^{-1} K^{-1} at room temperature.[11] Because E/κ ($\propto 1/C\tau$, where C is heat capacity and τ is phonon scattering time) is indicative of the phonon scattering rate, the high ratios observed for the ESOs demonstrate the use of entropy stabilization with multiple components to reduce phonon scattering times rather than velocities, which opens the door to unique combinations of properties, in this case simultaneously high elastic modulus and near-minimum thermal conductivity.

To better understand this reduction in thermal conductivity from 5- to 6-cations, we measure the thermal conductivities of J14 and J35 over a temperature range of 78 - 450 K, presented in Fig. 3(a). J14 and J35 have nearly identical average mass, thickness, and sound speed, making the two ideal candidates to compare. A similar reduction in thermal conductivity is observed in J35 compared to J14 at all temperatures tested. Unlike typical crystalline materials' thermal conductivity trends with temperature, both J14 and J35 display trends indicative of amorphous materials, having increasing thermal conductivities with temperature. To put this into perspective, we measure the thermal conductivity of a-J14 to show this characteristic amorphous thermal conductivity relation with temperature, revealing that J35 shows similar magnitudes of thermal conductivity to those of a-J14 at comparable temperatures. Furthermore, we measure 2-cation oxides of $Cu_{0.2}Ni_{0.8}O$, $Zn_{0.4}Mg_{0.6}O$, $Co_{0.25}Ni_{0.75}O$ at 230 - 450 K to show the characteristic Umklapp scattering trend ($\propto 1/T$) expected in crystalline materials and enhanced thermal conductivity relative to J14/J35. Qualitatively, the addition of cations results in greater deviation from a perfect crystal, which reduces thermal conductivity through increased phonon scattering. We model this phonon scattering to estimate the thermal conductivity as a function of temperature using the virtual crystal approximation (VCA)[30], details and assumptions for which are provided in the Supporting Information.
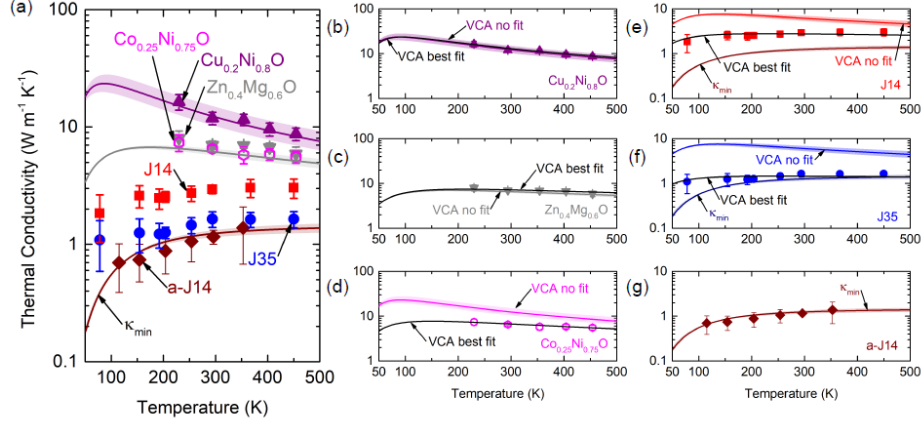
FIG. 3. (a) Thermal conductivity vs. temperature. Purple and gray lines depict VCA models without fitting parameters for $Cu_{0.2}Ni_{0.8}O$ and $Zn_{0.4}Mg_{0.6}O$, while maroon line is the minimum thermal conductivity model for J14 (κ_{min}); shaded regions indicate uncertainties in the model. Thermal conductivity data is shown together with VCA models with and without adjustable parameters for (b) $Cu_{0.2}Ni_{0.8}O$, (c) $Zn_{0.4}Mg_{0.6}O$, (d) $Co_{0.25}Ni_{0.75}O$, (e) J14 (f) J35, and (g) a-J14.

Assessing the VCA as a predictive model, Fig. 3 shows that it accurately describes the thermal conductivity relation with temperature for both (b) $Cu_{0.2}Ni_{0.8}O$ and (c) $Zn_{0.4}Mg_{0.6}O$ when considering only mass disorder as the phonon-defect scattering process. The VCA, while capturing the Umklapp scattering temperature trend observed experimentally, does not accurately predict the magnitude of thermal conductivity for (d) $Co_{0.25}Ni_{0.75}O$, owing to the nearly identical mass of Co and Ni, suggesting the need to include additional phonon scattering due to variations in the interatomic force constants (IFCs). For the purposes of the VCA analytical model, we treat the IFC scattering rate coefficient and the Grüneisen parameter, which affects normal scattering rates, as fitting parameters. With these adjustable parameters, the VCA can accurately capture the measured thermal conductivity, as depicted in Fig. 3(d). Addition of these fitting terms proves to make a negligible difference for (b) $Cu_{0.2}Ni_{0.8}O$ and (c) $Zn_{0.4}Mg_{0.6}O$. Overall, the VCA captures the thermal conductivity of these 2-cation oxides with reasonable agreement to experiment.

When applied to 5- and 6-component ESOs, the VCA lacks predictive capability in both magnitude and temperature trend; this is shown in Fig. 3(e) and (f) for J14 and J35, respectively. In fact, the VCA predicts that J14 and J35 should have higher thermal conductivities than both

$Zn_{0.4}Mg_{0.6}O$ and $Co_{0.25}Ni_{0.75}O$ due their virtual crystal's average mass having a smaller weighted difference with constituent masses than do the 2-component oxides. Indeed, a saturation of phonon scattering from mass disorder limits the thermal conductivity reduction achievable with an increasing number of components.[31] A similar argument can be made regarding additional terms describing disorder scattering in the VCA, which are likewise defined by the difference between average and constituent properties. While fitting parameters allow for better agreement between the VCA and experimental thermal conductivities, no combination of Grüneisen parameter and IFC scattering rate can capture the amorphous-like temperature trend. However, this amorphous-like trend has been observed in a variety of complex crystalline systems.[23] In such cases, the minimum thermal conductivity (κ_{min}) model[19] can be invoked to lend insight into experimental findings. We show in Fig. 3(g) that κ_{min}, as defined for J14 based on sound speed derived from CR-AFM, agrees well with experimental thermal conductivities for a-J14 and reasonably captures J35's thermal conductivity.

That the VCA fails to capture the trend in thermal conductivity of J14 and J35 may be interpreted by recent developments by Seyf *et al.*,[32] who hypothesize that non-propagating modes (diffusons) can comprise the majority of vibrational modes contributing to thermal conductivity when disorder becomes large. This manifests itself in amorphous-like thermal conductivity trends with temperature. Moreover, we do not observe any statistically significant size effects in thermal conductivity for the samples tested here (see Supporting Information), further supporting the idea that either diffusons or short mean-free-path phonons/propagons dominate thermal transport in these systems. An alternative interpretation, however, is that if the VCA is valid, the temperature-independent Rayleigh scattering may be large enough to overwhelm Umklapp scattering. Indeed, if we remove Umklapp scattering from the VCA model, we can reasonably emulate the thermal conductivity as a function of temperature, suggesting that Rayleigh scattering is the dominant phonon scattering mechanism dictating thermal conductivity (see Supporting Information). Finally, although strong anharmonic phonon scattering has been shown to arise due to large mass disorder,[33] the thermal expansion coefficient for the ESOs are measured via temperature-dependent XRD to be $\sim 1.2-1.4 \times 10^{-5}/°C$, in agreement with constituent oxides MgO[34] and NiO,[35] suggesting anharmonic scattering is not abnormally strong in the ESOs. Therefore, the temperature-independent nature of the mechanism causing reduction in thermal conductivity in ESOs, in particular that driving down 5- to 6-cation thermal conductivities, suggests strong Rayleigh scattering resulting from IFC disorder. The best-fit VCA models reveal that IFC disorder-

induced scattering must be $\sim 2.8\times$ higher in J35 than in J14 to account for the difference in thermal conductivities between the two. We emphasize that J14 and J35 have approximately the same average mass. Additionally, we systematically increase mass disorder among 6-component oxides via increasing 6th-cation mass (Fig. 1(f)) to conclude that while this increase leads to a reduction in thermal conductivity, the variation is less than 20%, far from the level of reduction needed to explain the difference from that of J14. Therefore, we hypothesize that there is a strong IFC disorder mechanism driving the enhanced reduction in thermal conductivity. Such a mechanism should be observable via differences in the local structure within the unit cell of J14 and J35.

To test this hypothesis, we use extended X-ray absorption fine structure (EXAFS)[36–39] to observe changes in the local coordination environment about Co absorbers in J14 and J35. While XRD revealed crystallographic order, EXAFS allows for an atomic-level probe of the local crystal structure needed for determination of any observable quantity that would reveal such IFC disorder. Figure 4 shows fits to the phase-uncorrected, self-absorption corrected magnitude and imaginary part of the real space function $\chi(R)$ for (a) J14 and (b) J35, obtained by taking the Fourier transform of the EXAFS spectra, $k^2\chi(k)$, using a Keiser-Bessel window in the range of 3.75 - 10 Å^{-1}. Each $\chi(R)$ is consistent with a typical metal-oxide system, where the first and second peaks correspond to scattering between the absorber and atoms in the first and second coordination shells, respectively. Figure 5 illustrates the modified unit cell for both (a) J14 and (b) J35 compositions extracted by EXAFS. For J14, we find an expected distortion of the Co octahedra that coincides with the observed lattice parameters of the tetragonal unit cell, $a = 4.21$ Å and $c = 4.29$ Å. By the second coordination shell, or absorber-metal scattering paths, we find that the half-path length agrees with observed lattice parameters within less than 1%. The addition of a 6th component, as is the case in J35, appears to dramatically change the absorber octahedra such that a geometric extension no longer aligns to the lattice parameters. J35 exhibits a tetragonally compressed unit cell, with $a = 4.21$ Å and $c = 4.08$ Å. Half scattering path lengths between the Co absorber and the six nearest neighboring oxygen atoms suggest a highly compressed octahedra with 4 planar oxygens at 1.93 Å and 2 axial oxygens at 1.96 Å. Again, comparing the half scattering path length of the next nearest neighbors agrees with observed lattice parameters to within 1%. These EXAFS results largely align with our hypothesis from the thermal measurements in that a large strain is present in the 6-component ESOs such that the oxygen atoms are displaced from their ideal coordination positions. Such strong oxygen sublattice distortion is the indicator that IFC disorder is greatly enhanced in J35 relative to J14. This strong IFC disorder is promoted by charge
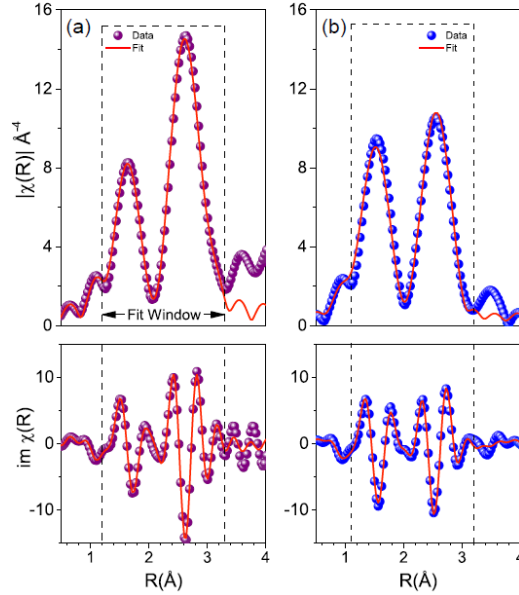
10

FIG. 4. Local structure determination. Extended X-ray absorption fine structure data and models about cobalt for (a) J14 and (b) J35. Model and best fit model are shown for the magnitude (top) and imaginary portion of the real space function $\chi(R)$ as a function of radius away from the cobalt absorber (R).

compensation among cations to preserve charge neutrality when a 6th cation is added.[40]

The attribution of thermal conductivity reduction in ESOs to interatomic force disorder is further supported by molecular dynamics simulations (see Supporting Information) in which IFC disorder is modeled by electrostatic point charges in the interatomic potential based on Bader charges from density functional theory calculations. These simulations reveal that accounting for differences in interatomic forces homogeneously through adjustment of average properties, analogous to the VCA, cannot capture magnitude or trend in thermal conductivity, whereas heterogeneous integration of mass and charge disorder accurately captures the reduction in thermal conductivity observed between J14 and 6-cation oxides, reducing the thermal conductivity by a factor of almost two, in agreement with experiment. Moreover, in these simulations we decouple mass and charge disorder to show that the latter is responsible for the strong reduction in thermal conductivity measured. Taken together, the experiment and simulation reveal that entropy-stabilized oxides can have a uniquely low thermal conductivity while maintaining a relatively high elastic modulus,
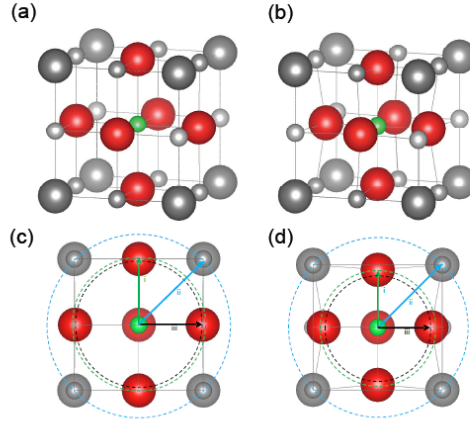
FIG. 5. Modified local structure of J14 and J35. Illustration depicting local structural changes about the cobalt species in (a) J14 and (b) J35. A comparison of the changes as a result of adding the 6th cation can be viewed by unit cell cross section along the (200) plane, as shown in (c) and (d) for J14 and J35 respectively. The lowercase roman numerals mark the coordination shell radius for i. nearest neighbor anion, ii. next nearest neighbor anion, and iii. nearest neighbor cation. In both cases, the nearest neighbor cation shell radius corresponds to one-half the face diagonal of the unit cell parameters, as determined through XRD.

made possible through highly disordered interatomic forces resulting from charge disorder among ionic bonds. These results provide an example of the broader aspect of entropy stabilization as a means to create materials with unique thermophysical properties that could be highly beneficial to thermoelectric and thermal barrier coating applications.

Experimental Section

Time- and Frequency-Domain Thermoreflectance: We use a combined time- and frequency-domain thermoreflectance (TDTR and FDTR) method, which is an optical pump-probe technique, to simultaneously measure the thermal conductivity and volumetric heat capacity of the thin-film ESO samples. This approach is based on the concept of varying the modulation frequency of the heating event to change the measurement property from thermal effusivity to thermal diffusivity, thereby decoupling thermal conductivity from volumetric heat capacity, allowing for a unique measurement of both quantities.[41–43] We extend the approach by Wei *et al.*[43] to incorporate TDTR phase data over a range of frequencies sufficient for FDTR, so as to combine the benefits of multifrequency TDTR and FDTR for thermal property measurement. This development provides a robust approach for measuring both the heat capacity and thermal conductivity of thin films.

Using the output of a pulsed Ti:Sapphire oscillator emanating 200 fs pulses at a repetition rate of 80 MHz, we divide the beam into two paths, a pump path and a probe path. The pump is used to heat a sample of interest, which has an 80 nm aluminum layer of aluminum deposited on it to serve as a transducer to convert the optical energy to thermal energy. The probe is used to measure the in-phase and out-of-phase change in thermoreflectance resulting from the pump-induced heating at time delays ranging from 200 ps to 6 ns and modulation frequencies ranging from 500 kHz to 10 MHz. A lock-in amplifier is used to ensure data collection at a given modulation frequency and improve signal-to-noise ratios. The number of data points collected are chosen such that they are sufficient for TDTR at a given frequency and pulsed-pulsed FDTR at a given probe time delay. Using a multilayer, radially symmetric thermal model incorporating both time delay and modulation frequency information directly extending from TDTR analysis procedures,[44–46] we use a surface fitting method to minimize the residuals between a time- and frequency-dependent thermal model with experimental data by varying three thermal parameters: ESO volumetric heat capacity (C_v), ESO thermal conductivity (κ), and Al/ESO thermal boundary conductance ($G_{Al/ESO}$). The ESO/MgO thermal boundary conductance ($G_{ESO/MgO}$) can in principle be set as a fitting parameter as well. However, in practice we are generally insensitive to this parameter, such that doing so gives us no additional benefit or physically meaningful information. Further details on the combined TDTR/FDTR approach and its comparison to the alternative methods to simultaneously measure C_v and κ can be found in the Supporting Information.

Extended X-ray Absorption Fine Structure: Extended x-ray absorption fine structure (EXAFS) spectra were collected at beamline 10-BM-B at the Advanced Photon Source, Argonne National

Laboratory (Lemont, IL). The Co K-edge was measured in fluorescence mode using a 4-element Vortex detector, elevated 30° above the sample. Measurement parameters varied by region of interest, determined by signal at higher k values up to ∼12 Å, as described elsewhere.[47] Individual scattering paths from Co absorbers are generated in J14 and J35 using FEFF6,[48] and fit to $\chi(R)$ using Artemis.[49] All EXAFS related uncertainty values were generated though the least squares output from fitting results.

Quantitatively, we obtain local structural information of the first and second nearest neighbors by fitting a theoretical model to the uncorrected $\chi(R)$ between ∼1-3.1 Å using a Kaiser-Bessel window, including all scattering path lengths that fall within this range. The structural model used for fits is based on information obtained though X-ray diffraction, shown in Fig. 1(a), exhibiting a single phase, tetragonally strained rocksalt structure pinned in-plane to the MgO substrate. Each fit generally contains four fitting parameters: amplitude reduction factor S_0^2, inner potential energy shift E_0, half scattering path distance R, and EXAFS Debye-Waller factor σ^2. The resulting best-fit values for which are listed in Table S2 (see Supporting Information).

Contact Resonance Atomic Force Microscopy: Contact resonance atomic force microscopy (CR-AFM) measurements were performed on a MultiMode 8 AFM (Bruker, Santa Barbara, CA, USA) equipped with a lock-in amplifier (Signal Recovery AMETEK, Oak Ridge, TN, USA) for CR frequency measurements. The AFM probes used were integrated PPP-SEIH silicon tips (Nanosensors, Neuchatel, Switzerland) with the first two free resonance frequencies at 102.0 kHz and 637.9 kHz and cantilever spring constant of 6.9 N/m. The same load of 84 nN was applied on the tip-sample contact in all the measurements to directly observe the stiffness response of the second CR frequency shift within a fix frequency range from 900.0 kHz to 1,200.0 kHz with a step of 50 Hz. A lock-in detection technique was used to measure the change in the CR frequency during these sweeps. A set of five measurements were made on each material, with two sets of measurements on sapphire bracketing the measurements on the ESO test materials. This measurement cycle with sapphire as reference was to confirm that the tip did not sustain wear or damage during measurements. Indeed, no significant deviations were observed in the measured CR frequencies on sapphire and all the measurements were used in the subsequent analysis. Besides these CR-AFM of the second eigenmode, a separate set of measurements were performed on all the materials studied with frequency sweeps over a larger range (100.0 kHz to 1,200.0 kHz, step 100 Hz) to observe both first and second CR frequencies. From these measurements, it was confirmed that the cantilever is well described by a spring coupled-clamped beam model with the

tip located at the end of the beam.[50, 51] By using this beam model, the frequencies measured on each material were normalized to the first free resonance of the cantilever and used to calculate the normalized contact stiffnesses. With the assumption of a Hertz contact geometry, these contact stiffnesses and the indentation moduli of the reference and AFM tip were used to determine the indentation modulus of a given material.[50–52] For each material, the measured second CR frequencies were used to calculate a weighted average and uncertainty of this average with the weights given by the uncertainties of the measured frequencies (the half width at the half height of the resonance peak). The uncertainty for each determined elastic modulus was calculated then by adding in quadrature the independent uncertainties from the first free-resonance of the cantilever and the second CR frequencies on the tested ESO sample and on the reference material, respectively.[51] The substrate contribution to the calculated elastic moduli was found negligible for the contact geometry, film thickness, applied loads, and materials involved in these measurements. *Disclaimer:* Certain commercial equipment, instruments, or materials are identified in this document. Such identification does not imply recommendation or endorsement by the National Institute of Standards and Technology, nor does it imply that the products identified are necessarily the best available for the purpose.

[1] J. W. Yeh, S. K. Chen, S. J. Lin, J. Y. Gan, T. S. Chin, T. T. Shun, C. H. Tsau, and S. Y. Chang, Advanced Engineering Materials **6**, 299 (2004).

[2] B. Cantor, I. T. H. Chang, P. Knight, and A. J. B. Vincent, Materials Science and Engineering: A **375–377**, 213 (2004).

[3] Y. J. Zhou, Y. Zhang, Y. L. Wang, and G. L. Chen, Applied Physics Letters **90**, 181904 (2007).

[4] M.-H. Tsai, C.-W. Wang, C.-W. Tsai, W.-J. Shen, J.-W. Yeh, J.-Y. Gan, and W.-W. Wu, Journal of the Electrochemical Society **158**, H1161 (2011).

[5] C.-C. Tung, J.-W. Yeh, T.-t. Shun, S.-K. Chen, Y.-S. Huang, and H.-C. Chen, Materials Letters **61**, 1 (2007).

[6] Y. L. Chou, Y. C. Wang, J. W. Yeh, and H. C. Shih, Corrosion Science **52**, 3481 (2010).

[7] Y.-F. Kao, T.-D. Lee, S.-K. Chen, and Y.-S. Chang, Corrosion Science **52**, 1026 (2010).

[8] M.-H. Chuang, M.-H. Tsai, W.-R. Wang, S.-J. Lin, and J.-W. Yeh, Acta Materialia **59**, 6308 (2011).

[9] H.-P. Chou, Y.-S. Chang, S.-K. Chen, and J.-W. Yeh, Materials Science and Engineering: B **163**, 184 (2009).

[10] C.-L. Lu, S.-Y. Lu, J.-W. Yeh, and W.-K. Hsu, Journal of Applied Crystallography **46**, 736 (2013).

[11] Z. Fan, H. Wang, Y. Wu, X. Liu, and Z. Lu, RSC Advances **6**, 52164 (2016).

[12] C. M. Rost, E. Sachet, T. Borman, A. Moballegh, E. C. Dickey, D. Hou, J. L. Jones, S. Curtarolo, and J.-P. Maria, Nat Commun **6** (2015).

[13] D. Berardan, S. Franger, A. K. Meena, and N. Dragoe, Journal of Materials Chemistry A **4**, 9536 (2016).

[14] S. Zhai, J. Rojas, N. Ahlborg, K. Lim, M. F. Toney, H. Jin, W. C. Chueh, and A. Majumdar, Energy & Environmental Science , (2018).

[15] R. Liu, H. Chen, K. Zhao, Y. Qin, B. Jiang, T. Zhang, G. Sha, X. Shi, C. Uher, W. Zhang, and L. Chen, Advanced Materials **29**, 1702712 (2017).

[16] X. Wang, C. D. Liman, N. D. Treat, M. L. Chabinyc, and D. G. Cahill, Physical Review B **88**, 075310 (2013).

[17] B. M. Foley, H. J. Brown-Shaklee, J. C. Duda, R. Cheaito, B. J. Gibbons, D. Medlin, J. F. Ihlefeld, and P. E. Hopkins, *Applied Physics Letters*, Applied Physics Letters **101**, 231908 (2012).

[18] L. Chen, J. L. Braun, B. F. Donovan, P. E. Hopkins, and S. J. Poon, *Applied Physics Letters*, Applied Physics Letters **111**, 131902 (2017).

[19] D. G. Cahill, S. K. Watson, and R. O. Pohl, Phys. Rev. B **46**, 6131 (1992).

[20] F. J. DiSalvo, Science **285**, 703 (1999).

[21] N. P. Padture, M. Gell, and E. H. Jordan, Science **296**, 280 (2002).

[22] C. Chiritescu, D. G. Cahill, N. Nguyen, D. Johnson, A. Bodapati, P. Keblinski, and P. Zschack, Science **315**, 351 (2007), http://science.sciencemag.org/content/315/5810/351.full.pdf.

[23] M. Beekman and D. G. Cahill, Crystal Research and Technology **52**, 1700114 (2017).

[24] W.-L. Ong, E. S. O'Brien, P. S. M. Dougherty, D. W. Paley, C. Fred Higgs III, A. J. H. McGaughey, J. A. Malen, and X. Roy, Nature Materials **16**, 83 EP (2016).

[25] D. T. Morelli, V. Jovovic, and J. P. Heremans, Physical Review Letters **101**, 035901 (2008).

[26] J. Ma, O. Delaire, A. F. May, C. E. Carlton, M. A. McGuire, L. H. VanBebber, D. L. Abernathy,

16

G. Ehlers, T. Hong, A. Huq, W. Tian, V. M. Keppens, Y. Shao-Horn, and B. C. Sales, Nature Nanotechnology **8**, 445 EP (2013).

[27] R. Vassen, X. Cao, F. Tietz, D. Basu, and D. Stöver, Journal of the American Ceramic Society **83**, 2023 (2000).

[28] Y. Zhang, T. T. Zuo, Z. Tang, M. C. Gao, K. A. Dahmen, P. K. Liaw, and Z. P. Lu, Progress in Materials Science **61**, 1 (2014).

[29] J. Yan, F. Liu, G. Ma, B. Gong, J. Zhu, X. Wang, W. Ao, C. Zhang, Y. Li, and J. Li, Scripta Materialia **157**, 129 (2018).

[30] B. Abeles, Phys. Rev. **131**, 1906 (1963).

[31] A. Giri, J. L. Braun, C. Rost-Barber, and P. E. Hopkins, Scripta Materialia **138**, 134 (2017).

[32] H. R. Seyf, L. Yates, T. L. Bougher, S. Graham, B. A. Cola, T. Detchprohm, M.-H. Ji, J. Kim, R. Dupuis, W. Lv, and A. Henry, npj Computational Materials **3**, 49 (2017).

[33] J. Garg, N. Bonini, B. Kozinsky, and N. Marzari, Phys. Rev. Lett. **106**, 045901 (2011).

[34] S. Isao, "Thermal expansion of periclase and olivine, and their anharmonic properties," in *Elastic Properties and Equations of State* (American Geophysical Union (AGU), 2013) pp. 361–375.

[35] J. Keem and J. Honig, *Selected electrical and thermal properties of undoped nickel oxide*, Tech. Rep. (DTIC Document, 1978).

[36] S. Calvin, *Igarss 2014*, 1 (CRC, Boca Raton, 2014) pp. 1–5, arXiv:arXiv:1011.1669v3.

[37] G. S. Knapp, M. V. Nevitt, A. T. Aldred, and T. K. Klippert, Journal of Physics and Chemistry of Solids **46**, 1321 (1985).

[38] S. Velu, K. Suzuki, C. S. Gopinath, H. Yoshida, and T. Hattori, Physical Chemistry Chemical Physics **4**, 1990 (2002).

[39] D. Grandjean, H. L. Castricum, J. C. Van Den Heuvel, and B. M. Weckhuysen, in *AIP Conference Proceedings*, Vol. 882 (2007) pp. 636–638.

[40] Z. Rak, C. M. Rost, M. Lim, P. Sarker, C. Toher, S. Curtarolo, J. P. Maria, and D. W. Brenner, *Journal of Applied Physics*, Journal of Applied Physics **120**, 095105 (2016).

[41] A. J. Schmidt, R. Cheaito, and M. Chiesa, Review of Scientific Instruments **80**, 094901 (2009).

[42] J. Liu, J. Zhu, M. Tian, X. Gu, A. Schmidt, and R. Yang, Review of Scientific Instruments **84**, 034902 (2013).

[43] C. Wei, X. Zheng, D. G. Cahill, and J.-C. Zhao, *Review of Scientific Instruments*, Review of Scientific Instruments **84**, 071301 (2013).

[44] D. G. Cahill, Review of Scientific Instruments **75**, 5119 (2004).

[45] P. E. Hopkins, J. R. Serrano, L. M. Phinney, S. P. Kearney, T. W. Grasser, and C. T. Harris, Journal of Heat Transfer **132**, 081302 (2010).

[46] A. J. Schmidt, X. Chen, and G. Chen, Review of Scientific Instruments **79**, 114902 (2008).

[47] C. M. Rost, Z. Rak, D. W. Brenner, and J.-P. Maria, Journal of the American Ceramic Society **100**, 2732 (2017).

[48] M. Newville, Journal of Synchrotron Radiation **8**, 322 (2001), arXiv:arXiv:1011.1669v3.

[49] B. Ravel and M. Newville, Journal of Synchrotron Radiation **12**, 537 (2005).

[50] U. Rabe, K. Janser, and W. Arnold, Review of Scientific Instruments **67**, 3281 (1996).

[51] G. Stan and W. Price, *Review of Scientific Instruments*, Review of Scientific Instruments **77**, 103707 (2006).

[52] G. Stan and R. F. Cook, Nanotechnology **19**, 235701 (2008).

Supporting Information

Charge Induced Disorder Controls the Thermal Conductivity of Entropy Stabilized Oxides

Jeffrey L. Braun,* Christina M. Rost, Mina Lim, Ashutosh Giri, David H. Olson, George Kotsonis, Gheorghe Stan, Donald W. Brenner, Jon-Paul Maria, and Patrick E. Hopkins*

1. MODELING THE THERMAL CONDUCTIVITY

A. Theory

Derived from the Boltzman transport equation under the relaxation time approximation,[1–4] the thermal conductivity is $\kappa = \frac{1}{3}\sum_j \int C_j(\omega)v_j^2(\omega)\tau_j(\omega)\,\mathrm{d}\omega$, where C is mode specific heat capacity, ω is phonon angular frequency, v is phonon group velocity, τ is phonon relaxation time, and j denotes phonon polarization. Intrinsic scattering processes involve phonon-phonon scattering, which include momentum conserving Normal and momentum destroying Umklapp processes ($\propto \omega^2$), and Rayleigh scattering from mass and strain impurities resulting from, for example, natural isotopes and point defects ($\propto \omega^4$). Extrinsic boundary scattering can result from sample dimensions being on the order of phonon mean free paths; for a thin film this takes the form $\tau_b = 2v_j/d$, where d is the film thickness. For random alloys and solid solutions, Abeles developed the virtual crystal approximation (VCA),[5] whereby a random alloy is treated as an effective crystal possessing the compositionally- weighted average properties (sound speed, mass, atomic radii, dispersion, intrinsic scattering rates) of the elements or compounds constituting the virtual crystal; additional phonon scattering results from differences in constituent and virtual crystal properties. In general, these Rayleigh scattering mechanisms are derived from perturbation theory,[6] such that their use, and the phonon gas picture in general, become dubious when disorder becomes large.[7] Still, this formalism has been used to adequately model the thermal conductivity in a variety of materials, including SiGe,[5, 8, 9] InGaN[10], InAsP,[5] and GaInAs[5] across a range of compositions, and remains the standard to model alloy thermal conductivity, even within first principles frameworks.[11] Under the VCA, Rayleigh scattering is proportional to $\Gamma = \Gamma_m + \Gamma_f$ and is described by Abeles to be $\Gamma = \sum_i x_i[(\Delta m/\bar{m})^2 + 2((\Delta G/\bar{G}) - 2 \times 3.2\gamma(\Delta\delta/\bar{\delta}))^2]$, where x is the concentration of each species, γ is an average anharmonicity of bonds, and the difference in mass (m), stiffness constant of nearest neighbor bonds (G), and atomic radii (δ) are with respect to their average respective quantities ($\bar{m}, \bar{G}, \bar{\delta}$). The disorder defining Γ can take many forms, including mass, strain, interatomic force constant (IFC), and charge disorder. Because the latter three are related, we decouple Γ into mass disorder (Γ_m) and interatomic force (Γ_f) disorder terms. Further details are provided below.

B. Model Details

We model the thermal conductivity, κ, as a function of temperature, using the relation

Equation S1

$$\kappa = \frac{1}{3}\sum_j \int_0^{k_{\max}} \hbar\omega_j(k)D_j(k)\frac{\partial f(k)}{\partial T}v_j^2(k)\tau_j(k)\,\mathrm{d}k,$$

where k is the phonon wavevector, j is an index that refers to the polarization (longitudinal/transverse, acoustic/optical), $\hbar$ is the reduced Planck's constant, ω is the phonon angular frequency, D is the phonon density of states, f is the phonon equilibrium distribution function (Bose-Einstein distribution), T is temperature, v is the phonon group velocity ($\partial\omega/\partial k$), and τ is the phonon relaxation time. Integration in Equation (S1) is performed in phonon wavevector space to allow the use of numerical dispersion relations for MgO and NiO obtained from literature.[12, 13] However, in practice we find that Debye approximation, the standard for dispersion modeling of alloys whose phonon contribution to thermal conductivity is typically assumed to be dominated by low-frequency modes, is sufficient for modeling these systems.

The relaxation time τ for a bulk crystal, such as MgO or NiO, is a combination of isotope/impurity scattering[3] (τ_I) as well as Normal and Umklapp scattering[1, 3, 14-16] (τ_N and τ_U). τ_I is proportional to ω^4, while τ_N and τ_U share the same ω^2 dependence, so that we combine them into a single term. Together, the phonon relaxation time becomes

Equation S2
$$\tau_j^{-1} = \tau_{I,j}^{-1}(k) + \tau_{N,j}^{-1}(k) + \tau_{U,j}^{-1}(k) = A\omega_j^4(k) + BT\omega_j^2(k)\exp(-C/T),$$

where A, B, and C are constants that are typically assigned based on a best-fit of Equation S1 to experimental data. In this case, we use experimental thermal conductivity data vs. temperature for MgO[17] and NiO[18] to fit these constants using both an actual dispersion as well as a Debye dispersion. The resulting experimental data and fit are shown in Figure S1; similarly good fits are found for both the full dispersion and Debye dispersion. In the former case, A = 1.86×10^{-38} s^3, B = 4.61×10^{-19} s K^{-1}, and C = 80.3 K for MgO, while A = 4.02×10^{-48} s^3, B = 5.68×10^{-19} s K^{-1}, and C = 41.0 K for NiO. In the latter case, A = 1.12×10^{-39} s^3, B = 9.20×10^{-19} s K^{-1}, and C = 146.3 K for MgO, while A = -8.51×10^{-49} s^3, B = 1.24×10^{-18} s K^{-1}, and C = 81.66 K for NiO. We note that the fitted values for A in each case were negligible in determining the best-fit; changing this value by several orders of magnitude made little difference to the fit. Moreover, when these constants are used later to model the 2-, 5-, and 6-component systems, the mass scattering, which takes the same ω^4 form, overwhelmingly outweighs any A obtained for the bulk crystal.
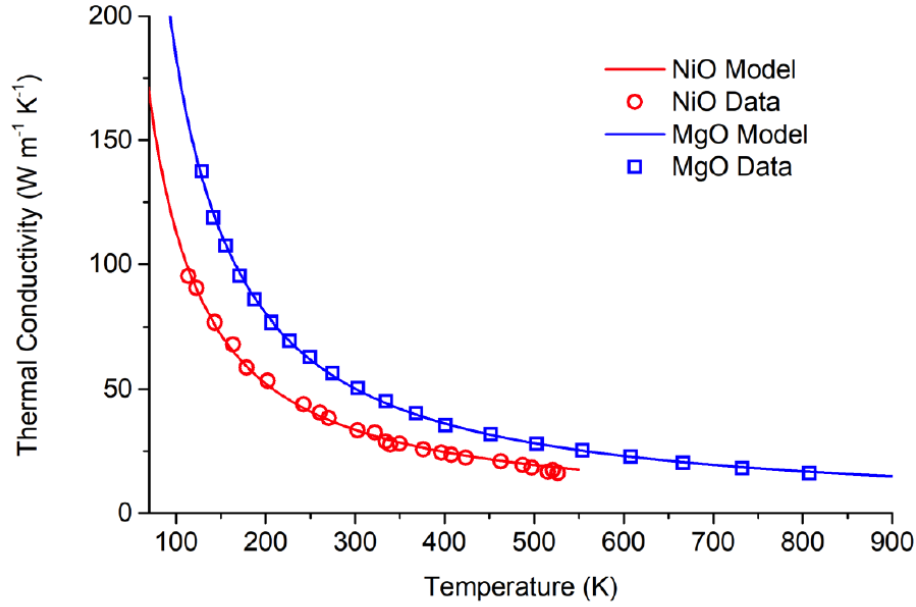
Figure S1. Thermal conductivity vs. temperature for MgO and NiO. Models depict the thermal conductivity calculated by Equation S1 with best-fit values for parameters A, B, and C.

To extend this model to multi-component systems, we add the additional scattering times due to mass-impurity scattering[19] (τ_m), normal scattering, [10, 14] and boundary scattering (τ_b) resulting from finite film thicknesses (d) in experimental samples. Using Matthiessen's rule, the total scattering time, τ, takes the form

Equation S3

$$\tau_j^{-1} = \tau_{I,j}^{-1}(k) + \tau_{m,j}^{-1}(k) + \tau_{U,j}^{-1}(k) + \tau_{N,j}^{-1}(k) + \tau_{b,j}^{-1}(k)$$

$$= \left(A + \frac{\Gamma\Omega}{12\pi v_j^3(k)} \right) \omega_j^4(k) + \left(B + \frac{k_B \gamma^2 \Omega^{1/3}}{\overline{m} v_j^3} \right) T\omega_j^2(k) \exp\left(-\frac{C}{T} \right) + \frac{2v_j(k)}{d}$$

where the mass-impurity is a Rayleigh type scattering in which phonon-displacement, phonon-isotope impurity, and phonon-mass impurity scattering are included in Γ. k_B is Boltzmann's constant, γ is the Grüneisen parameter describing the average anharmonicity between bonds, and Ω is the volume per atom. Γ is described by[5]

Equation S4

$$\Gamma = \Gamma_m + \Gamma_f = \sum_i x_i \left[\left(\frac{\Delta m_i}{\overline{m}} \right)^2 + 2\left(\left(\frac{\Delta G_i}{\overline{G}} \right) - 2 \times 3.2\gamma \left(\frac{\Delta \delta_i}{\overline{\delta}} \right) \right)^2 \right],$$

where x_i is the fraction of element i, m_i denotes the atomic mass of species i, G_i represents the average stiffness constant of nearest neighbor bonds of species i within the host lattice, and δ_i denotes atomic radius of species i. Under the VCA, $\overline{m}$, $\overline{G}$, and $\overline{\delta}$ are the average mass, stiffness, and atomic radius of the perturbed atoms, in this case the metal cations. From this

3

analytical expression, we observe that three terms dictate the Rayleigh scattering of phonons within a multi-component alloy or solid solution: (1) mass difference, (2) bond strength difference, and (3) atomic radii difference between impurity and host atom. While the mass differences are easily quantifiable, the latter terms, which are all related to the interatomic force constants, are not. Therefore, we split the summation in Equation (S4) to distinguish the contribution from mass and interatomic forces, $\Gamma = \Gamma_m + \Gamma_f$. We can then model the thermal conductivity with and without the Γ_f term to assess its contribution to the model.
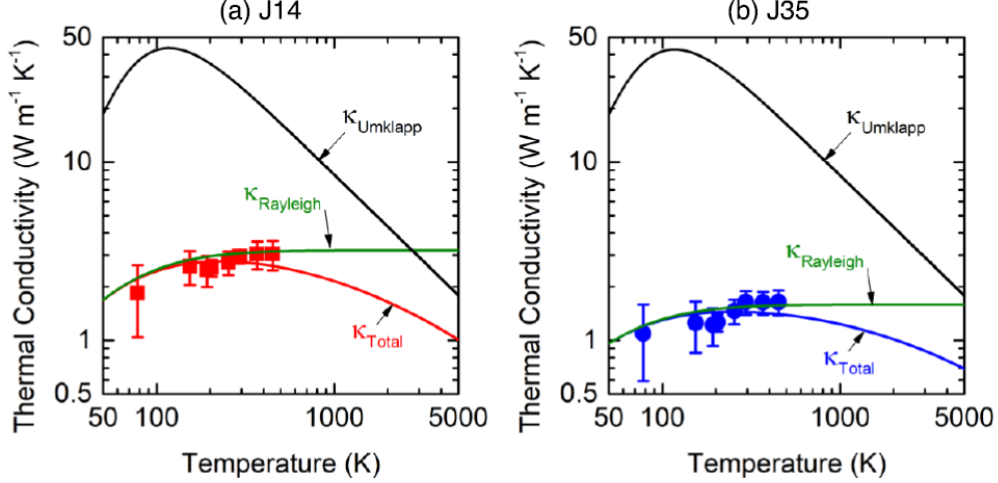
Figure S2. Thermal conductivity vs. temperature for (a) J14 (squares) and (b) J35 (circles), together with the best fit VCA model, κ_{Total}, which is described by Equation S1 and contains both Umklapp and Rayleigh scattering rates in the model. $\kappa_{Umklapp}$ shows the model when Rayleigh scattering is turned off and Umklapp scattering is on, while $\kappa_{Rayleigh}$ shows the model when Rayleigh scattering is turned on and Umklapp scattering is off.

Under the VCA, all cations are assumed to have the same mass equal to the average cation mass, $\bar{m}$, such that mass differences in Equation (S4) are with respect to $\bar{m}$. Additionally, the differences in stiffness constants and atomic radii are with respect to those average quantities of all cations. In this case, the B and C used in Equation (S2) will take the form of the average B and C for each oxide constituent. However, we estimate these values based on the average of only two such components, MgO and NiO, due to the lack of rigorous temperature dependent thermal conductivity data for single crystal forms of the other constituents. Nonetheless, we find that this approximation B and C is relatively unimportant because the other scattering terms dominate the total scattering time of the system. We use the VCA with the relaxation time described by Equation (S3) to calculate the models. We begin with no fitting parameters, ignoring Γ_f in Eq S4 and assuming the Grüneisen parameter is that of MgO (1.6). Uncertainty in the VCA is primarily from uncertainty in this Grüneisen parameter controlling the normal scattering rate, which we vary from 1.2 to 2.0 based on the constituent oxide values. We then fit for Γ_f and γ. All model parameters are listed in Table S1.

4

Table S1. Model parameters for VCA under a Debye approximation: γ is the Grüneisen parameter, Γ_f is the strain portion of Γ, B and C are Umklapp scattering parameters.

Sample	B (s K^{-1})	C (K)	Γ_f (no fit)	γ (no fit)	Γ_f (best fit)	γ (best fit)
J14	1.08×10^{-18}	114	0	1.6 ± 0.4	0.496	0
J35	1.08×10^{-18}	114	0	1.6 ± 0.4	1.39	0
$Co_{0.2}Ni_{0.8}O$	1.24×10^{-18}	81.6	0	1.6 ± 0.4	0.0015	1.43
$Zn_{0.4}Mg_{0.6}O$	0.92×10^{-18}	146.3	0	1.6 ± 0.4	0	0.84
$Co_{0.25}Ni_{0.75}O$	1.24×10^{-18}	81.6	0	1.6 ± 0.4	0.11	1.34

The resulting models with and without fitting parameters are shown in Figure 3 of the main text. However, in order to justify our claim that the Rayleigh scattering mechanism is dominant over Umklapp scattering, we show the model with and without Rayleigh scattering in Figure S2. The total thermal conductivity, κ_{Total}, represents the best fit model and considers both Umklapp scattering and Rayleigh scattering. $\kappa_{Umklapp}$ shows the model when Rayleigh scattering is turned off and Umklapp scattering is on, while $\kappa_{Rayleigh}$ shows the model when Rayleigh scattering is turned on and Umklapp scattering is off. The model describing $\kappa_{Umklapp}$ greatly overestimates the thermal conductivity and always possesses a decreasing thermal conductivity trend with temperature at elevated temperatures. However, considering Rayleigh scattering without Umklapp scattering, the model describing $\kappa_{Rayleigh}$ better captures the experimental data. This finding suggests that Rayleigh scattering is the dominant phonon scattering mechanism dictating the thermal conductivity in ESOs within the temperature range tested.

The minimum limit to thermal conductivity was determined using[20]

Equation S5

$$\kappa_{\min} = \left(\frac{\pi}{6}\right)^{1/3} k_B n^{2/3} \sum_j v_j \left(\frac{T}{\theta_j}\right)^2 \int_0^{\theta_j/T} \frac{x^3 e^x}{(e^x - 1)^2}\, dx,$$

where n is number density and $\theta_j = v_j (\hbar/k_B)(6\pi^2 n)^{1/3}$. The sound speeds, v_j, used to calculate $\kappa_{\min}$ are listed in Table S3. For ESO samples, these values are derived from the measured elastic modulus.

2. MEASURING HEAT CAPACITY AND THERMAL CONDUCTIVITY SIMULTANEOUSLY

Transient techniques used to measure thermal conductivity, such as time and frequency-domain thermoreflectance (TDTR/FDTR), are generally analyzed with the heat diffusion equation so that the volumetric heat capacity and thermal conductivity are coupled through the thermal effusivity or thermal diffusivity, depending on the time and length scales of the heating event. Typically for alloys and solid solutions, a composition-weighted average is used to estimate volumetric heat capacity. However, recent developments in thermoreflectance experiments have enabled simultaneous measurements of both heat capacity and thermal conductivity of thin films. The conditions for doing so are outlined and validated in previous studies[21–23], all of which rely on the same operating principle of varying the modulation frequency to decouple the sensitivity of the measurement to thermal conductivity and heat capacity, but are carried out in different ways. There have been many demonstrations of this concept using both FDTR[21, 24, 25], and TDTR at multiple modulation

frequencies [22, 23, 26–30]. In this study, we use and compare all of these approaches to characterize the thermal conductivity and volumetric heat capacity simultaneously, when experimental conditions allow. Additionally, we extend the approach by Wei et al.[23] to incorporate TDTR phase data over a range of frequencies sufficient for FDTR, so as to combine the benefits of multifrequency TDTR and FDTR for thermal property measurement. This development provides a robust approach for measuring both the heat capacity and thermal conductivity of thin films. We mention the caveat that we are able to decouple the thermal conductivity and heat capacity only as much as experimental conditions allow. Because the samples tested here are thin films on a conductive substrate (MgO), the thermal penetration depth can be very high, such that the ESO sample becomes thermally thin[26] so that the ratio is sensitive to thermal conductivity but less sensitive to the volumetric heat capacity. Operating in this regime allows us to characterize the thermal conductivity with larger sensitivity than volumetric heat capacity; as a result, the measurement of heat capacity comes with large uncertainty. This concept becomes especially important at low temperatures where the thermal conductivity of the MgO substrate is so high that the thin film is thermally thin relative to the total thermal penetration depth.

We use the surface fitting procedure discussed in the main text to extract thermal conductivity and volumetric heat capacity. Figure S3 shows the best fit model and data for J14. Fitting parameters include the Al/ESO thermal boundary conductance ($G1 \approx 170$ MW m^{-1} K^{-1}), thermal conductivity (κ), and volumetric heat capacity (C_v). The ESO/MgO thermal boundary conductance (G_2) was taken to be 300 MW m^{-1} K^{-1}; fitting this additional parameter gave the same value, but because we are insensitive to it, fitting this parameter does not provide additional benefit. The best fit surface is shown together with the experimental phase data in Figure S3(a), while Figure S3(b) and (c) show the corresponding time and frequency domain best fit models and data to reveal that the combination of fitted values works well to describe the data at all time and frequency points.
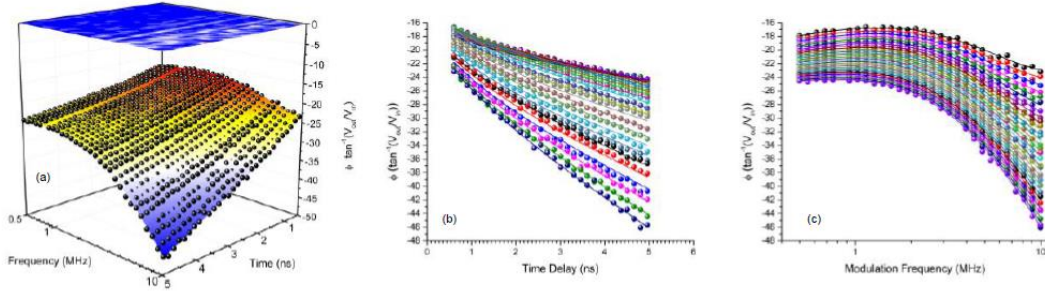
Figure S3. (a) J14 combined TDTR and FDTR experimental phase data and best-fit surface. (b) Time-domain data and best fit models. (c) Frequency-domain data and best fit models. In all cases, the best fit model is that of the surface fit minimization.
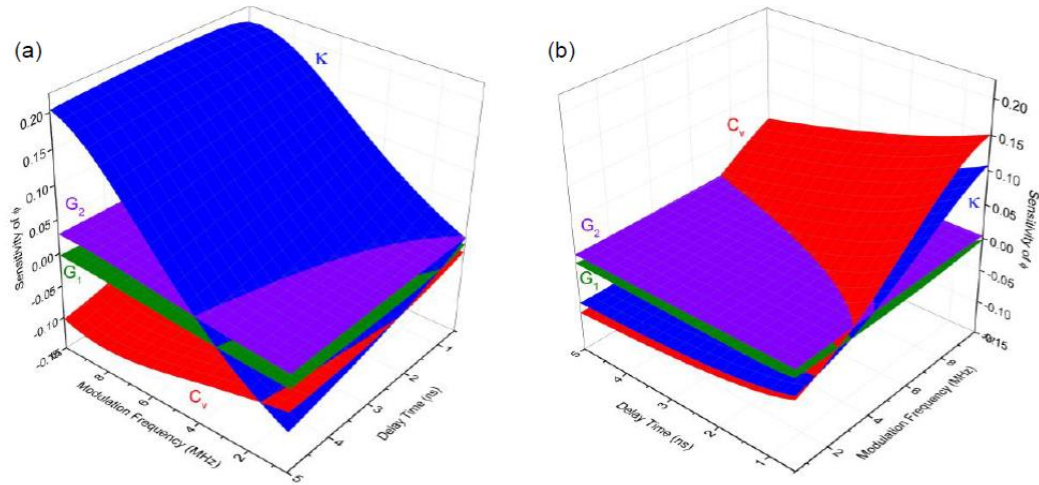
Figure S4. Sensitivity of phase (φ) for (a) 114 nm J14 and (b) 78 nm amorphous J14 (a-J14) as a function of delay time and modulation frequency for thermal conductivity (κ), volumetric heat capacity (C_v), Al/J14(a-J14) thermal boundary conductance (G_1) and J14(a-J14)/MgO(a-SiO$_2$) thermal boundary conductance (G_2).

Whereas the thermal boundary conductances and input parameters can generally be assumed independent variables in terms of their affect on the fitted parameters' uncertainties[31], we recognize that κ and C_v are coupled, motivating the use of the contour approach by Wang et al.[26] to quantify their respective role on the total uncertainty. To obtain the contours for thermal conductivity determined in Figure 1 of the main text, we determine the combinations for κ and C_v that produce a model that falls within $2\sigma_{min}$, defined as[26]

Equation S6

$$\sigma_{min} = \sum_{j=1}^{q} \frac{\sum_{i=1}^{n} \left(\frac{\phi_{m,i} - \phi_{d,i}}{\phi_{d,i}} \right)^2}{n},$$

7

where ϕ_m is the model for the phase or ratio, ϕ_d is the experimental data for the phase or ratio, q is the number of modulation frequencies used, and n is the number of time points used. This contour approach reveals that for J14 and the 6-component oxides, C_v and κ can be simultaneously obtained. One notes, however, that C_v has a higher percentage uncertainty than does κ. This can be explained based on the sensitivity of the fitting parameters within the thermal model, R, used. The sensitivity to a parameter x is defined as[32]

Equation S7

$$S_x = \frac{\partial \ln(R)}{\partial \ln(x)} \, ,$$

The sensitivity is dependent on both time and modulation frequency. The sensitivity to phase is shown for 114 nm J14 at room temperature in Figure S4(a) to reveal that C_v and κ have significantly different sensitivities in both magnitude and trend across all delay times and modulation frequencies, which allows us to decouple the two quantities using the surface fitting procedure. Because the magnitude of sensitivity for κ is in general higher than that of C_v, the uncertainty in C_v is relatively larger; this is evidenced by the contour plot shown in Figure 1(c) of the main text, in which a relatively wide range of volumetric heat capacities can be assumed to fit a relatively narrow range of thermal conductivities. The 6-component oxides show similar sensitivities to J14. As a result, we are able to simultaneously measure the κ and C_v, but with a relatively large uncertainty in C_v. For amorphous J14 (a-J14) and polycrystalline J14 (p-J14), which were grown on amorphous silicon dioxide substrates, we are not able to reliably decouple the heat capacity from thermal conductivity. The sensitivity explains this as well; shown in Figure S4(b) is the sensitivity for a-J14, which reveals that κ and C_v have near identical values and trends over all delay times and temperature. This indicates that the two quantities cannot be decoupled, because the two have near-identical effects on the model.

As mentioned previously, other approaches have been used to simultaneously measure the κ and C_v in thermoreflectance experiments. One of which, FDTR, was used here as well. We find that in general, FDTR at a single time delay gives similar fitted parameters as the combined TDTR/FDTR approach. We show this in Figure S5, where for J14 and all 6-component oxides, FDTR measurements were taken at five delay times (1 - 5 ns). The best fit models and data, together with the extracted κ and C_v, are shown for (a) J14, (b) J30, (c) J31, (d) J34, (e) J35, and (f) J36. FDTR proves to be reliable for thermal conductivity measurements in general, for the same reason regarding sensitivity to this parameter mentioned above. C_v measurements are in general in agreement with the combined FDTR/TDTR approach, but can be highly dependent on the delay time chosen, as evidenced by (a) J14 and (e) J35, which could be due to differing sensitivities or experimental noise. Thus, the combined TDTR/FDTR approach has the advantage of fitting over a broad range of data to negate some of these issues from individual FDTR scans, thus reducing some of the artifacts that may overwhelm the determination of small differences in thermal conductivities between samples (e.g. the 6-component oxides). Moreover, the combined TDTR/FDTR approach allows us to quantify the interdependent κ and C_v uncertainties via contour plots, which in general relies on both time- and frequency-dependent data.[26]

We next used the approach by Liu et al.[22] to vary C_v and fit κ at three frequencies. Figure S6 shows the resulting best fit values for κ as a function of C_v. The crossing point is taken to be the "true" thermal conductivity and heat capacity. In this case, we used three frequencies that span a range large enough to make the dominant thermal property measured transition from

8

film effusivity (highest frequency) to diffusivity (mid-frequency) to the lowest frequency case where the substrate properties become more influential. These regimes are evidenced by the differing trends of κ with C_v for each frequency for (a) J14, (b) J30, (c) J31, (d) J34, (e) J35, and (f) J36. In general, this approach gives similar values to the combined TDTR/FDTR approach, but it is clear that this approach is not as rigorous, and may require user judgement to find the crossing point. Taking J34 as an example, the 10 MHz line crosses the 0.615 MHz line at ~3.0 MJ m^{-3} K^{-1}, but crosses the 4.37 MHz line at ~3.7 MJ m^{-3} K^{-1}. The 0.615 MHz and 4.37 MHz lines also intersect at ~3.2 MJ m^{-3} K^{-1}. In this case, it may not be clear which value is the correct to use. On the other hand, for J36, all three frequency lines intersect once at ~3.5 MJ m^{-3} K^{-1}, in general agreement with the combined TDTR/FDTR approach. This approach, however, has a benefit of clearly showing when thermal conductivity and heat capacity cannot be decoupled. This can be seen in Figure S6(g) and (h) for p-J14 and a-14, respectively. All frequencies have the same κ vs. C_v relation, indicating that the two quantities cannot be independently measured under these experimental conditions.

Comparing the three approaches, we note that the combined TDTR/FDTR approach is the most rigorous and allows for a proper estimate of uncertainty when decoupling κ and C_v. Because of these benefits, we use this approach here to report measured values. We characterize J14 and J35 temperature-dependent data with this approach as well in order to extract κ and C_v as a function of temperature, using the same contour plots as we used at room temperature. Figure S7(a) shows the contour lines for the temperatures tested. Figure S7(b) shows the measured heat capacities as a function of temperature. In general, C_v falls within the range of C_v for each constituent oxide across all temperatures, with the exception of at 78 K. However, the large uncertainty at this temperature due to the J14's thermally thin nature and relatively high uncertainty in MgO substrate properties prevents us from accurately measuring this quantity. Finally, the thermal conductivities are shown as a function of temperature in Figure S7(c).

9
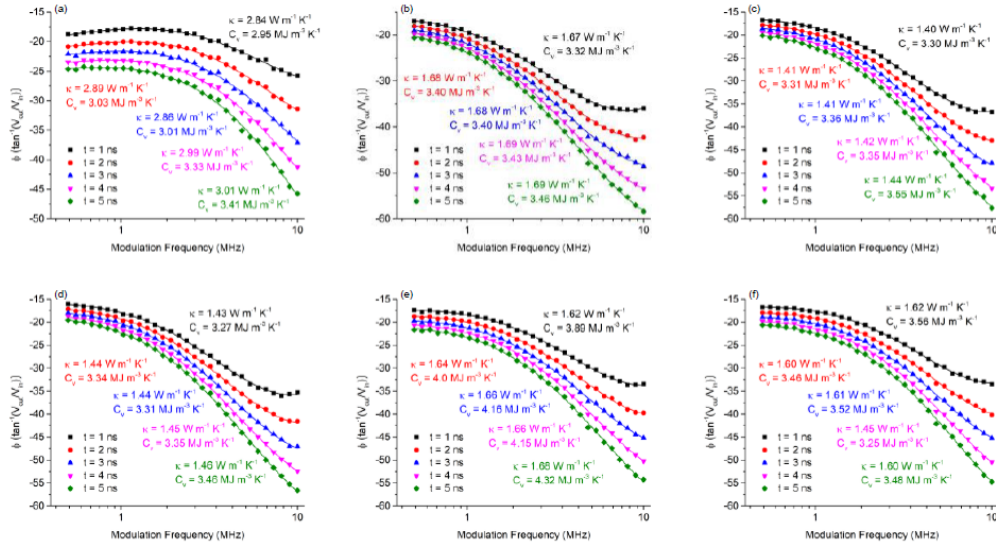
Figure S5. Best fit models and experimental FDTR data at five delay times for (a) J14, (b) J30, (c) J31, (d) J34, (e) J35, and (f) J36.
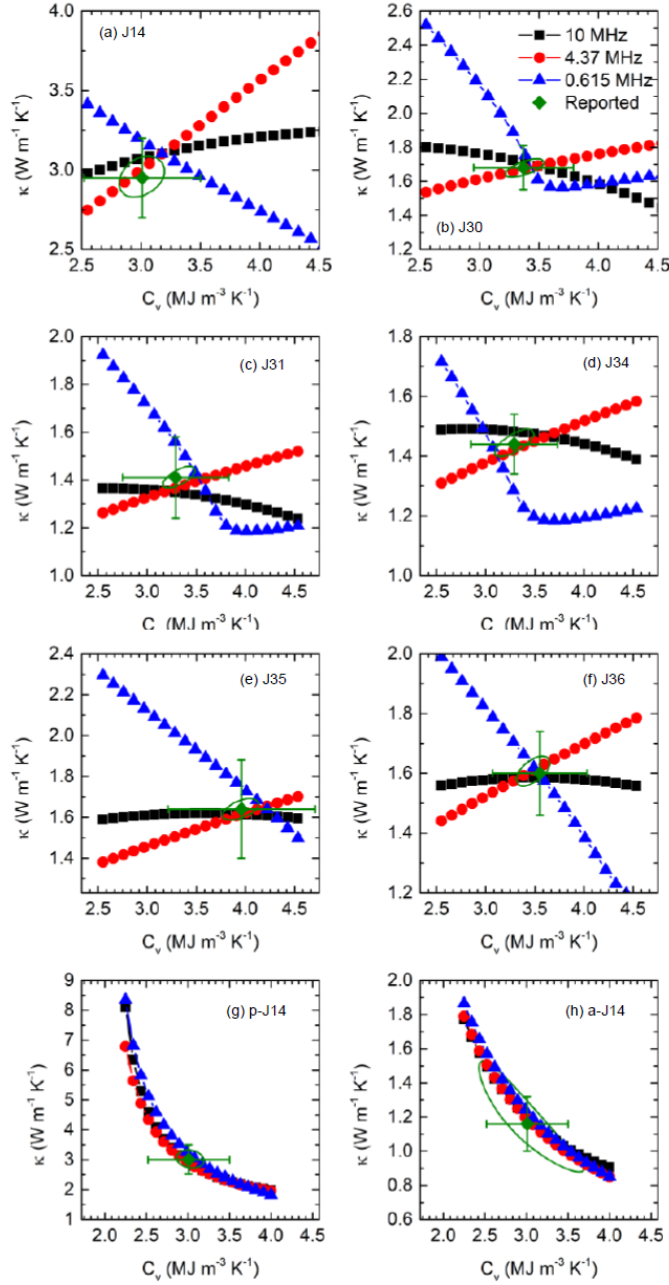
Figure S6. Best fit thermal conductivities as a function of volumetric heat capacity using the approach outlined by Liu et al.[22] for (a) J14, (b) J30, (c) J31, (d) J34, (e) J35, (f) J36, (g) polycrystalline J14, and (h) amorphous J14. To show the comparison to the values extracted via the combined TDTR/FDTR approach, also shown are the contours given in Figure 1(d) of the main text as well as the reported values including all propagated uncertainties.
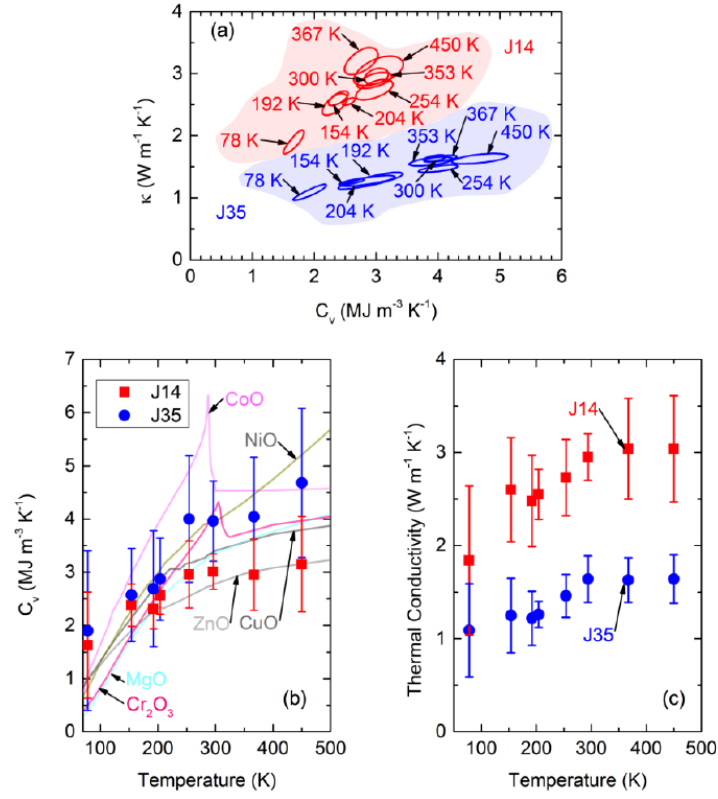
Figure S7. (a) Contour plot of thermal conductivity (κ) and volumetric heat capacity (C_v) for 114 nm J14 and 109 nm J35 over a range of temperature from 78 K to 450 K. (b) Measured C_v as a function of temperature for J14 and J35, together with literature values[33] of C_v for each constituent oxide to include MgO, NiO, CoO, ZnO, CuO, and Cr_2O_3. (c) Measured κ as a function of temperature for J14 and J35.

3. UNCERTAINTY ANALYSIS

In addition to the interdependent uncertainty of κ and C_v, there is additional uncertainty based on the uncertainties of input parameters to the thermal model. The uncertainty (δ) to a fitting parameter, x to an input parameter, y, is given by[23]

Equation S8

$$\left(\frac{\delta_x}{x}\right)^2 = \left(R * \frac{\delta\phi}{S_x}\right) + \sum \left(\frac{S_y}{S_x} * \frac{\delta_y}{y}\right)^2$$

where R is the signal (ratio or phase) and $\delta\phi$ is uncertainty in absolute phase of the RF lock-in amplifier. S_x denotes sensitivity to parameter x and the summation is over the total number input variables. Phase correction is post-processed[32, 34]. The RMS noise of the out-of-phase signal determines $\delta\phi$; for the modulation frequencies used in this study ($\geq$500 kHz), this RMS noise is small, so that in practice, only the latter term in Equation (S8) is important to calculate the uncertainty. The largest contributions to this term are the uncertainties in film thickness of the aluminum ($\pm$2 nm as determined by mechanical profilometry and picosecond acoustics) and film thickness of the ESO film (determined by x-ray reflectivity measurements, varies for each sample).
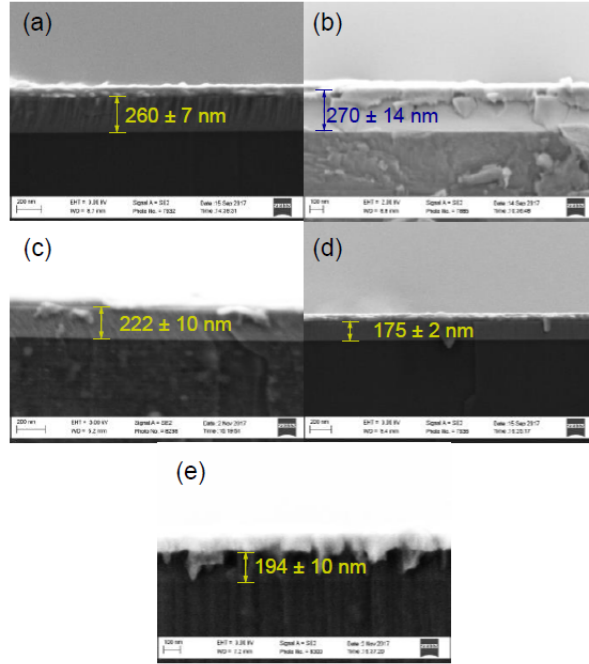
Figure S8. Cross-section SEM images of (a) J14, (b) J30, (c) $Cu_{0.2}Ni_{0.8}O$, (d) $Co_{0.25}Ni_{0.75}O$ and (e) $Zn_{0.4}Mg_{0.6}O$.

4. TESTING FOR SIZE EFFECTS IN THERMAL CONDUCTIVITY

To test for size effects, additional films of roughly double the thickness were deposited for J14 and J30. Cross-section scanning electron microscopy (SEM) was used to measure the film thicknesses of these samples and the 2-cation samples. The SEM images are shown in Figure S8. J14 was measured to be 260 nm ± 7 nm, while J30 was measured to be 270 nm ± 14 nm. Both of these films are about twice the thickness of the films discussed in the main text; thus, we should measure a higher thermal conductivity in the thicker samples compared to the ~100 nm samples if boundary scattering is significantly reducing phonon mean free paths. However, we measure 260 nm J14's thermal conductivity to be 3.17 ± 0.45 W m^{-1} K^{-1} and 270 nm J30's thermal conductivity to be 1.63 ± 0.23 W m^{-1} K^{-1}. Both of these values fall within the thermal conductivity uncertainty of their ~100 nm counterparts, which were reported in the main text as 2.95 ± 0.25 W m^{-1} K^{-1} and 1.68 ± 0.13 W m^{-1} K^{-1}, for 114 nm J14 and 149 nm J30, respectively. The J14 film was additionally measured as a function of temperature to reveal similar thermal conductivities as it's thinner counterpart. The lack of size effects on thermal conductivity indicates that the reported thermal conductivities are intrinsic values.

14

Table S2. Resulting parameter values from EXAFS analysis. All uncertainties are propagated though Artemis. S_0^2 is the amplitude reduction factor, E_0 is the inner potential energy shift, R is the half scattering path distance, and σ^2 is the EXAFS Debye-Waller factor.

Parameter	J14	J35
S_0^2	1.0	0.85
E_0	3.0 ± 1.0	2.0 ± 1.0
R	2.10 ± 0.02	1.96 ± 0.08
σ^2	0.0073 ± 0.0005	0.006 ± 0.002
R	2.15 ± 0.04	1.93 ± 0.04
σ^2	0.0073 ± 0.0005	0.006 ± 0.002
R	3.00 ± 0.01	2.86 ± 0.02
σ^2	0.0073 ± 0.0005	0.006 ± 0.002
R	-	2.97 ± 0.02
σ^2	-	0.006 ± 0.002

5. EXAFS FITTING PARAMETERS

The EXAFS fitting parameters are shown listed in Table S2. Each fit generally contains four fitting parameters: amplitude reduction factor S_0^2, inner potential energy shift E_0, half scattering path distance R, and EXAFS Debye-Waller factor σ^2.

6. ELASTIC MODULUS MEASUREMENTS AND DERIVATION OF SOUND SPEED

Contact resonance atomic force microscopy (CR-AFM)[35, 36] was used to determine the elastic moduli of all ESO samples. The measurements consisted of observing the change in the CR frequency, $f_2^{contact}$, of the second eigenmode of the cantilever under a given applied load on the tip-sample contact. By using the spring coupled-clamped beam model with the tip located at the end of the beam,[35, 37] the $f_2^{contact}$ frequencies measured on each material were normalized to the first free resonance f_1^{air} of the cantilever and used to calculate the normalized contact stiffness k/k_c, with k being the contact stiffness and k_c being the cantilever spring constant. With the assumption of a Hertz contact geometry, the contact stiffnesses and the indentation moduli of the reference and AFM tip were used to determine the indentation modulus of a given material,[35, 37, 38] $M_S = [(k_R/k_S)^{3/2}/M_R + (k_R/k_S)^{3/2}/M_T - 1/M_T]^{-1}$. The indices S, R, and T denote "sample" (the ESO test material), "reference" (sapphire) and "tip" (silicon), respectively. The determined indentation modulus was converted to Young's elastic modulus by assuming a Poisson ratio of 0.28 for each ESO material, $E_S = (1 - v_S^2)M_S$. Other values used were $E_R = 345.0$ GPa and $v_R = 0.29$ for sapphire, $E_T = 130.0$ GPa and $v_T = 0.28$ for the silicon tip. The substrate contribution to the determined elastic moduli was found negligible for the contact geometry, film thickness, applied loads, and materials involved in these measurements. For each material, the measured CR frequencies were used to determine a weighted average and uncertainty of this average with the weights given by the uncertainties Δf of the measured frequencies (the half width at the half height of the resonance peak). The uncertainty for each determined elastic modulus was calculated then by adding in quadrature the independent uncertainties from f_1^{air} (first free-resonance in air), $f_{2,S}^{contact}$ (second CR frequency on a test ESO sample), and $f_{2,S}^{contact}$ (second CR frequency on the reference material),[37]

Equation S9

$$\Delta E_S = \sqrt{\left(\frac{\partial E_S}{\partial f_1^{air}}\right)^2 \left(\Delta f_1^{air}\right)^2 + \left(\frac{\partial E_S}{\partial f_{2,S}^{contact}}\right)^2 \left(\Delta f_{2,S}^{contact}\right)^2 + \left(\frac{\partial E_S}{\partial f_{2,R}^{contact}}\right)^2 \left(\Delta f_{2,R}^{contact}\right)^2}$$

Figure S9 shows the second contact resonance frequency on sapphire (used as a calibration) and several ESO samples to demonstrate the differences observed that directly relate to the elastic moduli of these samples; higher frequencies are indicative of stiffer materials. The elastic moduli (E) among ESOs vary from ~150 to 250 GPa. From these elastic moduli, under the assumption that the elastic properties are isotropic and the Poisson's ratio (v) is 0.28, the longitudinal (v_L) and transverse (v_T) sound speeds can be derived from the following equations[29]

Equation S10

$$v_L = \sqrt{\frac{E(1 - v)}{\rho(1 + v)(1 - 2v)}},$$

16

Equation S11

$$v_T = \sqrt{\frac{G}{\rho}} = \sqrt{\frac{E}{2\rho(1+\nu)}},$$

where ρ is the density (assumed as the theoretical density) and G is the shear modulus. The resulting sound speeds are listed in Table S3.

Table S3. Longitudinal (v_L) and transverse (v_T) sound speeds in [100] direction for the oxide constituent oxides that make up J14.

Sample or Constituent	v_L [km s^{-1}]	v_T [km s^{-1}]
J14, Mg$_x$Ni$_x$Cu$_x$Co$_x$Zn$_x$O, x = 0.2	5.63	3.11
J30, Mg$_x$Ni$_x$Cu$_x$Co$_x$Zn$_x$Sc$_x$O, x = 0.167	7.16	3.96
J31, Mg$_x$Ni$_x$Cu$_x$Co$_x$Zn$_x$Sb$_x$O, x = 0.167	5.33	2.94
J34, Mg$_x$Ni$_x$Cu$_x$Co$_x$Zn$_x$Sn$_x$O, x = 0.167	5.77	3.19
J35, Mg$_x$Ni$_x$Cu$_x$Co$_x$Zn$_x$Cr$_x$O, x = 0.167	5.49	3.03
J36, Mg$_x$Ni$_x$Cu$_x$Co$_x$Zn$_x$Ge$_x$O, x = 0.167	6.67	3.68
MgO	9.11[a]	6.59[a]
NiO	7.39[b]	3.36[b]
ZnO	6.09[c]	2.76[c]
CoO	6.30[d]	2.90[d]
CuO	5.20[e]	2.20[e]

[a] Reference 39; [b] Derived from phonon dispersion, reference 13; [c] Reference 40; [d] Derived from elastic properties, reference 41; [e] Derived from elastic properties, reference 42.
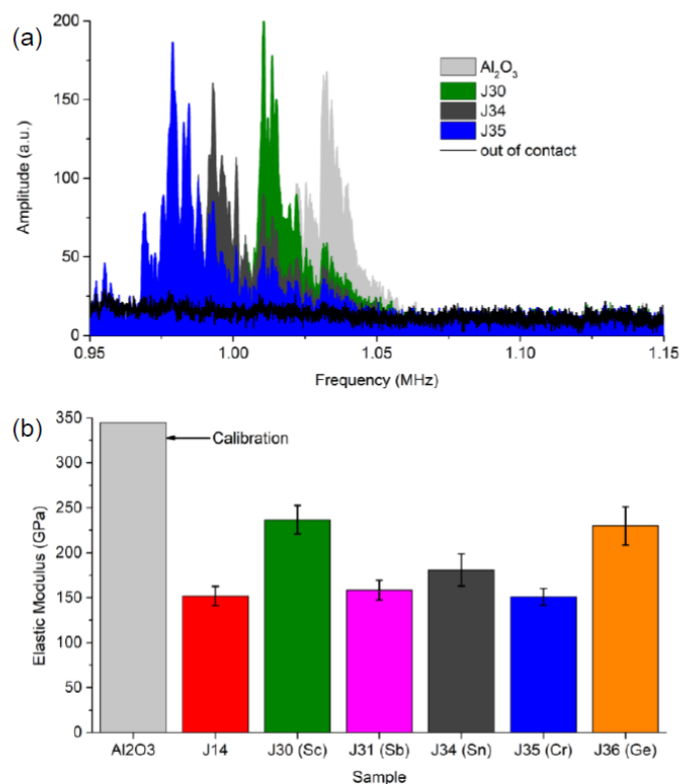
Figure S9. (a) The shift of the second contact resonance frequency on sapphire, J30, J34, and J35 respectively. The measurements were made under the same applied load, so the frequency shift reflects the stiffness of the material probe: Higher shifts on stiffer materials. The out-of-contact frequency spectrum shows the absence of any peak in this frequency range when the tip is not in contact with a material. (b) The determined Young's modulus of the samples probed by CR-AFM. The calculations were done by considering the sapphire as a reference material of Young's modulus 345.0 GPa and Poisson's ratio 0.29. An average Poisson's ratio of 0.28 was assumed for all the other materials. The uncertainty in the calculated elastic modulus of a material is the standard deviation of the mean value and includes the uncertainties in the contact frequencies measured on that material and on the reference. A set of five measurements were made on each material, with two sets of measurements on sapphire bracketing the measurements on the test materials.

## 7. LITERATURE DATA FOR ELASTIC MODULUS AND THERMAL CONDUCTIVITY

Table S4 lists the elastic moduli and thermal conductivity obtained from the listed references.

Table S4. Elastic moduli (E) and thermal conductivities (κ) for isotropic single crystals at room temperature.

Material	E [GPa]	κ [W m^{-1} K^{-1}]
Ag	87.03 [a]	429 [b]
Al	71.26 [a]	237 [b]
Au	89.15 [a]	317 [b]
Cu	144.57 [a]	401 [b]
Fe	227.48 [a]	80.4 [b]
W	389.02 [a]	174 [b]
K	4.51 [a]	102.4 [b]
Na	9.24 [a]	143 [b]
Ni	231.17 [a]	90.9 [b]
Pb	28.28 [a]	35.3 [b]
Ge	135.40 [a]	60.2 [b]
Si	165.82 [a]	149 [b]
Diamond (I/ IIa/ IIb)	1144.81 [a]	900/2320/1360 [b]
AgSbTe$_2$	49.49 [c]	0.68 [d]
PbTe	67.23 [e]	1.7 [d]
InAs	79.70 [f]	27 [g]
SrTiO$_3$	260.85 [h]	11 [i]
SnTe	65.36 [e]	8.2 [j]
SnTe:Ga, x=0.1	68.30 [e]	6.3 [j]
Ag$_8$SnSe$_6$	52.63 [k]	0.39 [k]
MgO	310 [l]	52 [m]
Al$_2$O$_3$	345 [m]	34 [m]
MAPbCl$_3$ (cubic)	23.0 [n]	0.73 [n]
MAPbBr$_3$ (cubic)	17.8 [n]	0.51 [n]
MAPbI$_3$ (tetragonal)	12.0 [n]	0.34 [n]
CsPbBr$_3$ (othorombic)	13.5 [n]	0.46 [n]
FAPbBr$_3$ (cubic)	10.2 [n]	0.49 [n]
YB$_{66}$	362.69 [o]	2.55 [p]
(KBr)$_{0.81}$ (KCN)$_{0.19}$	16.35 [q]	0.67 [p]

Co_6S_8	4.0 [r]	0.22 [r]
Co_6Se_8	2.3 [r]	0.18 [r]
Co_6Te_8	0.62 [r]	0.13 [r]
$[Co_6Se_8][C_{60}]_2$	8.1 [r]	0.25 [r]
$[Co_6Te_8][C_{60}]_2$	1.5 [r]	0.16 [r]
C_{60}	10 [s]	0.4 [t]
C_{70}	4 [s]	0.07 [t]
$BaZrO_3$	181 [u]	4.3 [u]
$La_2Zr_2O_7$	175 [u]	1.90 [u]
Y_2O_3-stabilized ZrO_2 (YSZ)	210 [u]	2.13 [u]
NiO	175 [v]	34 [w]
B_9C	350 [x]	3.9 [y]
$(BiSbTe_{1.5}Se_{1.5})_{1-x}Ag_x$, x = 0	72 [z]	0.66 [z]
$(BiSbTe_{1.5}Se_{1.5})_{1-x}Ag_x$, x = 0.3	58 [z]	0.59 [z]
$(BiSbTe_{1.5}Se_{1.5})_{1-x}Ag_x$, x = 0.6	39 [z]	0.61 [z]
$(BiSbTe_{1.5}Se_{1.5})_{1-x}Ag_x$, x = 0.9	60 [z]	0.51 [z]
$(BiSbTe_{1.5}Se_{1.5})_{1-x}Ag_x$, x = 1.2	58 [z]	0.57 [z]
AlCoCrFeNi	127 [aa]	11 [ab]
J14	152.0 [m]	2.95 [m]
J30	236.7 [m]	1.68 [m]
J31	158.4 [m]	1.41 [m]
J34	180.8 [m]	1.44 [m]
J35	151.0 [m]	1.64 [m]
J36	229.9 [m]	1.60 [m]

a) Reference 43; b) Reference 44; c) Reference 45; d) Reference 46; e) Reference 47;
f) Reference 48; g) Reference 49; h) Reference 50; i) Reference 51; j) Reference 52;
k) Reference 53; l) Reference 54; m) This study; n) Reference 55; o) Reference 56;
p) Reference 20; q) Reference 57; r) Reference 58; s) Reference 59; t) Reference 60;
u) Reference 61; v) Reference 62; w) Reference 18; x) Reference 63; y) Reference 64;
z) Reference 65; aa) Reference 66; ab) Reference 67
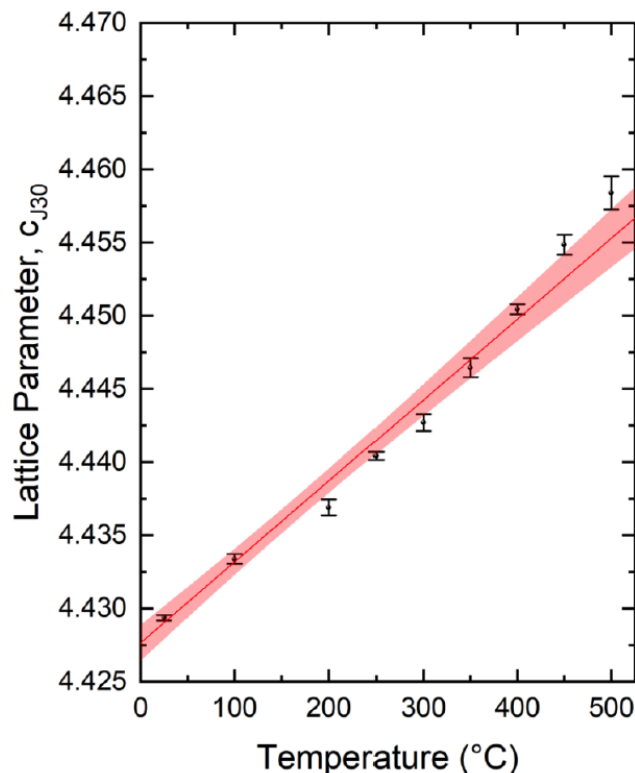
Figure S10. Lattice parameter of J30 vs. temperature. The line represents the best fit to the data and the shaded region represents the 95% confidence bounds.

8. COEFFICIENT OF THERMAL EXPANSION

The coefficient of thermal expansion (CTE) was measured for composition J30 via non-ambient XRD. A Panalytical Empyrean was equipped with an Anton-Paar HTK 1200N high-temperature oven chamber. To avoid any significant interfacial diffusion, high temperatures were primarily avoided. Measurements were taken incrementally between 25 °C and 500 °C in air around the (002) film and substrate peaks, respectively (39- 45 2θ). The ramp rate was 60 °C/min. and each measurement was taken within 10 degrees of incremental set points for a total measurement time of approximately 90 min. Using Bragg's law, the shift in diffraction angle was converted to unit cell lattice parameter and plotted as a function of temperature. Figure S10 shows the resulting trend for the expansion of the out-of-plane lattice parameter, c, of J30 as a function of temperature. From the slope of the linear fit and its relationship to CTE, we find the linear CTE of the out-of-plane lattice parameter of J30 to be $1.2 \pm 0.2 \times 10^{-5}$ K^{-1}, which agrees well with both the previously measured CTE of J14,[68] as well as nominal MgO[69] and NiO.[70]

21

9. MOLECULAR DYNAMICS SIMULATIONS

A. Charge induced interatomic force constant disorder

Molecular dynamics simulations were performed to further probe the relationship between thermal conductivity, composition, and the mass and IFC disorder. The potential energy function (φ) between atom i and j used in the simulations consisted of an exponential-6 pair potential

Equation S12

$$\phi_{ij} = A_{ij} \exp\left(-\frac{r_{ij}}{\rho}\right) - \frac{C_{ij}}{r_{ij}^6} + \frac{q_i q_j}{4\pi\varepsilon_0 r_{ij}}$$

where the last term is defines the electrostatic interactions modeled by atom-centered point charges. A, ρ and C are Buckingham potential parameters taken from prior work modeling MgO[71] while Bader charges from Density Functional Theory (DFT) calculations were used for the electrostatic point charges[72]. This model is not intended to quantitatively reproduce thermal conductivities, but rather to explore the explicit issue of the reduction in thermal conductivity with the addition of a sixth cation. Three compositions are reported here, J14, J30 (J14+Sc), and J35 (J14+Cr). For each system, a 480 atom unit cell was populated using the special quasi-random structure algorithm.[73] As described in detail elsewhere, DFT calculations were carried out in which the structure was relaxed to minimize the energy.[72] The point charges used in the simulations were then set equal to the Bader DFT charges (or their average values). The systems used in the simulations reported here each contained 4×4×4 unit cells for a total of 30,700 atoms.

Using the LAMMPS package,[74] the potential energy was first minimized with respect to atom position, followed by equilibration at zero pressure and 300 K for 32 picoseconds using a Nose-Hoover thermostat. After equilibration, the thermal conductivity was calculated under NVE conditions using the Green-Kubo method [75–77] for 20 nanoseconds. This was sufficient to produce a converged value of thermal conductivity for each system. To separate the effects of charge from mass disorder, four systems were simulated for each of the three compositions. The cases include (1) individual DFT charges and individual masses being distributed randomly to cation positions (heterogeneous charge / heterogeneous mass), (2) a single charge and mass for each ion that was equal to the average of the DFT charges and atomic mass, respectively (homogeneous charge / homogeneous mass), (3) a single charge and distributed individual masses (homogeneous charge / heterogeneous mass), and (4) distributed individual DFT charges and a single mass (heterogeneous charge / homogeneous mass). These average charge and mass values are given in Table S5.
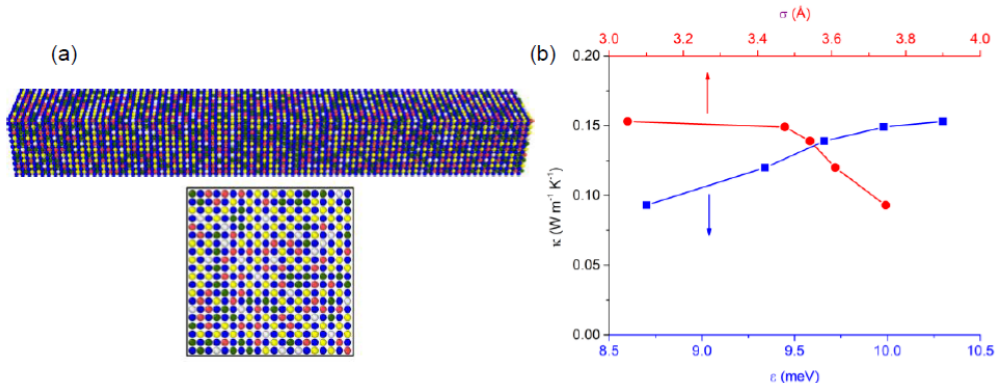
The calculated thermal conductivities for all 12 systems are given Table S5 and Figure S11. The introduction of a sixth cation reduces thermal conductivity compared to J14 for both Sc and Cr, in agreement with experiment. For the three compositions, heterogeneity in either mass or charge reduces the thermal conductivity compared to the corresponding fully homogeneous systems. However, there is little difference between heterogeneity in mass and charge, and heterogeneity in charge only. This suggests that scattering from disorder in the force constants dominates over that from scattering due to mass disorder. This agrees with our interpretation of the VCA model's ability to capture experimental data only when Rayleigh scattering from IFC disorder dominates the total phonon scattering rate dictating thermal conductivity.
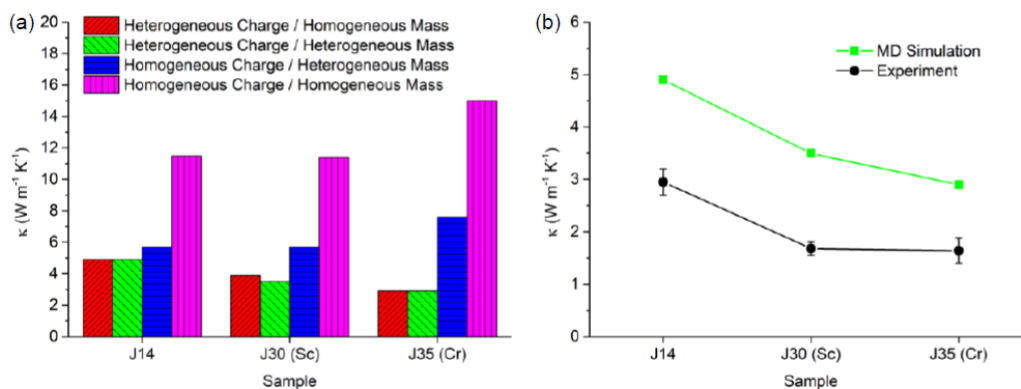
Figure S11. (a) Thermal conductivities obtained from equilibrium molecular dynamics simulations using all combinations of homogeneous and heterogeneous mass and charge. The scenario that includes heterogeneous charge and heterogeneous mass most closely captures experimental conditions. (b) Comparison of experimental thermal conductivities to MD results from the heterogeneous charge / heterogeneous mass case. The MD results capture the reduction in thermal conductivity measured experimentally.

Table S5. Thermal conductivity (κ) results from equilibrium molecular dynamics simulations.

Sample	κ [W m^{-1} K^{-1}] Heterogeneous charge/ Homogeneous mass	κ [W m^{-1} K^{-1}] Heterogeneous charge/ Heterogeneous mass	κ [W m^{-1} K^{-1}] Homogeneous charge/ Heterogeneous mass	κ [W m^{-1} K^{-1}] Homogeneous charge/ Homogeneous mass	Average Charge [e]	Average Mass [g mol^{-1}]
J14	4.9	4.9	5.7	11.5	1.285	47.09
J30	3.9	3.5	5.7	11.4	1.283	46.72
J35	2.9	2.9	7.6	15.0	1.333	47.84

Figure S12. (a) Schematic of computational domain and (b) thermal conductivity (κ) results from non-equilibrium molecular dynamics simulations vs. both parameters defining the LJ potential, ε (bottom axis) and σ (top axis).

B. Charge induced interatomic force constant disorder

In addition to the material specific potentials used to capture the experimentally observed trends in thermal conductivity, we also show that this concept of interatomic force disorder to reduce thermal conductivity can be generalized to other material systems. We employ the widely used 12-6 Lennard Jones (LJ) potential, $U(r) = 4\varepsilon[(\sigma/r)^{12} - (\sigma/r)^6]$, where U is the interatomic potential, r is the interatomic separation, and σ and ε are the LJ length and energy parameters, respectively. For computational efficiency the cutoff distance is set to 2.5σ for all the simulations and the time step is set to 1 fs throughout the simulations. As we are interested in understanding the general effect of mass and interatomic force constant disorder scattering on thermal transport in multi-atom component crystalline solid solutions as opposed to material specific properties, the use of the LJ potential is sufficient to provide this translational insight. For simplicity, the length and energy parameters are modeled for argon (σ = 3.405 Å and ε = 10.3 meV, respectively) with the lattice constant $a_0 = 1.56\sigma$ and arranged in an fcc lattice. The sizes of the computational domains are $10a_0 \times 10a_0 \times 80a_0$ with periodic boundary conditions applied in the x- and y- directions, whereas, fixed boundaries with 4 monolayers of atoms at each end are placed in the z-direction. The computational domain size was chosen to allow us to perform nonequilibrium molecular dynamics (NEMD) simulations. A schematic of the simulated structure is shown in Figure S12(a). In this case, an ordered sublattice of argon, shown as blue atoms, is analogous to oxygen anions in the ESO structures, while all other atoms have increasing integer multiples of argon mass from 2× to 5×. These additional atoms are randomly assigned to the remaining sublattice with equal probability, analogous to the random configuration of metal cations in the ESO structures.

The computational domains are equilibrated under the Nose-Hoover thermostat and barostat with a fixed number of atoms, volume, and temperature. The domains are then left in an isothermal-isobaric ensemble with the number of particles, pressure, and temperature of the system held constant for a total of 2 ns at 0 bar pressure. For the NEMD simulations, a fixed amount of energy is added per time step to a warm bath at one end of the computational domain and removed in equal amount from a cool bath at the other end. The length of the baths is set to $10a_0$ in the z-direction, and the dynamics are carried out under a micro-canonical, NVE, ensemble, with the number of particles (N), volume (V), and energy (E) held constant. After 2 ns, a steady-state temperature gradient in the z-direction is established by
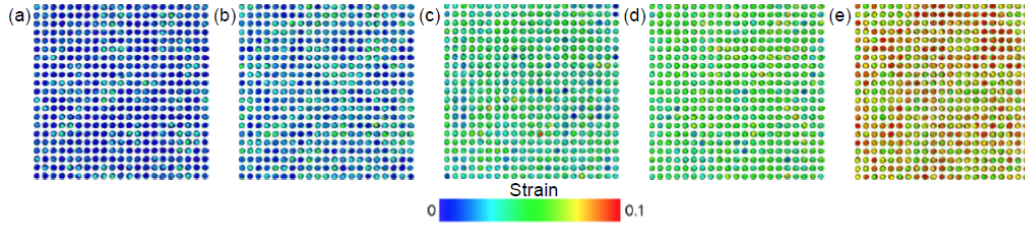
24

averaging the temperature for atoms in each monolayer for a total of another 5 ns. The thermal conductivity, κ is then determined by invoking Fourier's law, $Q = -\kappa(\partial T/\partial z)$ where the applied flux, Q, is in the z-direction.

Whereas the addition of further mass disorder in the form of higher integer multiples of argon mass makes a negligible difference in thermal conductivity,[78, 79] we find that adding interatomic force constant disorder can significantly reduce the thermal conductivity. We obtain such disorder by changing the LJ parameters, ε and σ, for all impurity atom species. Doing so effectively adds a random disruption to the otherwise continuous network of identical potentials defining the bond strength between atoms. Furthermore, we can change the strength of this disruption by changing the magnitude of difference in ε and σ relative to the baseline LJ parameters for argon. Figure S12(b) shows the resulting thermal conductivity change with adjusting the potential. The same results are also summarized in Table S6. There is a clear difference in thermal conductivity of over 50% between the lowest and highest value with the parameters chosen, confirming that stronger deviation from the baseline LJ potential leads to stronger reduction in thermal conductivity. However, like the experimental study on the ESOs, we need an observable metric that quantifies this disorder of interatomic forces. With the ESOs, we were able to use strain within the oxygen sublattice to reveal such disorder. Likewise, in these LJ systems, we use strain as a metric to quantify the disorder in interatomic forces. Shown in Figure S13 are snapshots of the von Mises strain[80, 81] on atoms with the 5 potentials listed in Table S6. We find that the average level of strain measured in these simulations is directly tied to the thermal conductivity extracted in NEMD simulations; the larger strain, indicative of larger interatomic force constant disorder as determined by deviation from the baseline LJ potential, corresponds to a stronger reduction in thermal conductivity.

Table S6. Thermal conductivity of nonequilibrium molecular dynamics simulations using Lennard Jones potentials with varying ε and σ parameters.

Label in Figure S13	ε [meV]	σ [Å]	κ [W m^{-1} K^{-1}]
(a)	10.30	3.05	0.153
(b)	9.98	3.47	0.149
(c)	9.66	3.54	0.139
(d)	9.34	3.61	0.12
(e)	8.70	3.75	0.093

Figure S13. Snapshots of the von Mises strain on atoms when parameters are adjusted within the LJ potential. The LJ parameters (ε and σ) and thermal conductivity (κ) for each case are (a) ε = 10.30 Å, σ = 3.05 meV, and κ = 0.153 W m^{-1} K^{-1}; (b) ε = 9.98 Å, σ = 3.47 meV, and κ = 0.149 W m^{-1} K^{-1}; (c) ε = 9.66 Å, σ = 3.54 meV, and κ = 0.139 W m^{-1} K^{-1}; (d) ε = 9.34 Å, σ = 3.61 meV, and κ = 0.12 W m^{-1} K^{-1}; (e) ε = 8.70 Å, σ = 3.75 meV, and κ = 0.093 W m^{-1} K^{-1}.

References

[1]   P. Klemens, in *Proceedings of the Royal Society of London A: Mathematical, Physical and Engineering Sciences* **1951**, 208, 108.
[2]   J. M. Ziman, *Can. J. Phys.* **1956**, 34, 1256.
[3]   J. Callaway, *Phys. Rev.* **1959**, 113, 1046.
[4]   P. G. Klemens, *Phys. Rev.* **1960**, 119, 507.
[5]   B. Abeles, *Phys. Rev.* **1963**, 131, 1906.
[6]   P. G. Klemens, in *Proceedings of the Physical Society. Section A* **1955**, 68, 1113.
[7]   H. R. Seyf, L. Yates, T. L. Bougher, S. Graham, B. A. Cola, T. Detchprohm, M.-H. Ji, J. Kim, R. Dupuis, W. Lv, and A. Henry, *npj Comput. Mater.* **2017**, 3, 49.
[8]   J. Garg, N. Bonini, B. Kozinsky, and N. Marzari, *Phys. Rev. Lett.* **2011**, 106, 045901.
[9]   D. G. Cahill, F. Watanabe, A. Rockett, and C. B. Vining, *Phys. Rev. B* **2005**, 71, 235202.
[10]   T. Tong, D. Fu, A. X. Levander, W. J. Schaff, B. N. Pantha, N. Lu, B. Liu, I. Ferguson, R. Zhang, J. Y. Lin, H. X. Jiang, J. Wu, and D. G. Cahill, *App. Phys. Lett.* **2013**, 102, 121906.
[11]   J. Carrete, B. Vermeersch, A. Katre, A. van Roekeghem, T. Wang, G. K. H. Madsen, and N. Mingo, *Comput. Phys. Commun.* **2017**, 220, 351.
[12]   K. Parlinski, J. Łaz̀ewski, and Y. Kawazoe, *J. Phys. Chem. Solids* **2000**, 61, 87.
[13]   R. Coy, C. Tompson, and E. Gurmen, *Solid State Commun.* **1976**, 18, 845.

[14]   C. Herring, *Phys. Rev.* **1954**, 95, 954.

[15]   M. G. Holland, *Phys. Rev.* **1963**, 132, 2461.

[16]   G. A. Slack and S. Galginaitis, *Phys. Rev.* **1964**, 133, A253.

[17]   D.G. Cahill, http://users.mrl.illinois.edu/cahill/tcdata/tcdata.html, accessed: 01, 2018

[18]   F. B. Lewis and N. H. Saunders, *J. Phys. C: Solid State Phys.* **1973**, 6, 2525.

[19]   P. E. Hopkins, *AIP Adv.* **2011**, 1, 041705.

[20]   D. G. Cahill, S. K. Watson, and R. O. Pohl, *Phys. Rev. B* **1992**, 46, 6131.

[21]   A. J. Schmidt, R. Cheaito, and M. Chiesa, *Rev. Sci. Instrum.* **2009**, 80, 094901.

[22]   J. Liu, J. Zhu, M. Tian, X. Gu, A. Schmidt, and R. Yang, *Rev. Sci. Instrum.* **2013**, 84, 034902.

[23]   C. Wei, X. Zheng, D. G. Cahill, and J.-C. Zhao, *Rev. Sci. Instrum.* **2013**, 84, 071301.

[24]   Y. Gao, A. M. Marconnet, R. Xiang, S. Maruyama, and K. E. Goodson, *IEEE Trans. Compon., Packag., Manuf. Technol.* **2013**, 3, 1524.

[25]   D. H. Hurley, R. S. Schley, M. Khafizov, and B. L. Wendt, *Rev. Sci. Instrum.* **2015**, 86, 123901.

[26]   X. Wang, C. D. Liman, N. D. Treat, M. L. Chabinyc, and D. G. Cahill, *Phys. Rev. B* **2013**, 88, 075310.

[27]   A. Giri, J.-P. Niemela, T. Tynell, J. T. Gaskins, B. F. Donovan, M. Karppinen, and P. E. Hopkins, *Phys. Rev. B* **2016**, 93, 115310.

[28]   X. Xie, D. Li, T.-H. Tsai, J. Liu, P. V. Braun, and D. G. Cahill, *Macromolecules* **2016**, 49, 972.

[29]   J. L. Braun, S. W. King, A. Giri, J. T. Gaskins, M. Sato, T. Fujiseki, H. Fujiwara, and P. E. Hopkins, *App. Phys. Lett.* **2016**, 109, 191905.

[30]   J. Liu, X. Wang, D. Li, N. E. Coates, R. A. Segalman, and D. G. Cahill, *Macromolecules* **2015**, 48, 585.

[31]   J. Yang, E. Ziade, and A. J. Schmidt, *Rev. Sci. Instrum.* **2016**, 87, 014901.

[32]   R. M. Costescu, M. A. Wall, and D. G. Cahill, *Phys. Rev. B* **2003**, 67, 054302.

[33]   Y. S. Touloukian, R. W. Powell, C. Y. Ho, and P. G. Klemens, "Thermophysical Properties of Matter - Specific Heat: Non-metallic Solids, Vol. 5," IFI/Plenum, New York, USA, **1970**.

[34]   A. J. Schmidt, *Optical Characterization of Thermal Transport from the Nanoscale to the Macroscale*, Ph.D. thesis, MIT, **2008**.

[35]   U. Rabe, K. Janser, and W. Arnold, *Rev. Sci. Instrum.* **1996**, 67, 3281.

[36]   K. Yamanaka and S. Nakano, *Jpn. J. Appl. Phys.* **1996**, 35, 3787.

[37]   G. Stan and W. Price, *Rev. Sci. Instrum.* **2006**, 77, 103707.

[38]   G. Stan and R. F. Cook, *Nanotechnol.* **2008**, 19, 235701.

[39]   A. Yoneda, *J. Phys. Earth* **1990**, 38, 19.

[40]   X. Wu, J. Lee, V. Varshney, J. L. Wohlwend, A. K. Roy, and T. Luo, *Sci. Rep.* **2016**, 6, 22504.

[41]   U. D. Wdowik and K. Parlinski, *Phys. Rev. B* **2007**, 75, 104306.

[42]   E. P. S. Tan, Y. Zhu, T. Yu, L. Dai, C. H. Sow, V. B. C. Tan, and C. T. Lim, *App. Phys. Lett.* **2007**, 90, 163112.

[43]   W. P. Mason, *Am. Inst. Phys. Handb.* **1972**, 104.

[44]   C. Y. Ho, R. W. Powell, and P. E. Liley, *J. Phys. Chem. Ref. Data* **1972**, 1, 279.

[45]   S. Berri, D. Maouche, and Y. Medkour, *Phys. B* **2012**, 407, 3320.

[46]   D. T. Morelli, V. Jovovic, and J. P. Heremans, *Phys. Rev. Lett.* **2008**, 101, 03590.

[47]   A. J. Miller, G. A. Saunders, and Y. K. Yogurtcu, *J. Phys. C: Solid State Phys.* **1981**, 14, 1569.

[48]   D. Gerlich, *J. App. Phys.* **1963**, 34, 2915.

[49]   P. D. Maycock, *Solid-State Electron.* **1967**, 10, 161.

[50]   R. O. Bell and G. Rupprecht, *Phys. Rev.* **1963**, 129, 90.

[51]   D.-W. Oh, J. Ravichandran, C.-W. Liang, W. Siemons, B. Jalan, C. M. Brooks, M. Huijben, D. G. Schlom, S. Stemmer, L. W. Martin, A. Majumdar, R. Ramesh, and D. G. Cahill, *App. Phys. Lett.* **2011**, 98, 221904.

[52]   R. Al Rahal Al Orabi, J. Hwang, C.-C. Lin, R. Gautier, B. Fontaine, W. Kim, J.-S. Rhyee, D. Wee, and M. Fornari, *Chem. Mater.* **2017**, 29, 612.

[53]   L. Li, Y. Liu, J. Dai, A. Hong, M. Zeng, Z. Yan, J. Xu, D. Zhang, D. Shan, S. Liu, Z. Ren, and J.-M. Liu, *J. Mater. Chem. C* **2016**, 4, 5806.

[54]   D.-H. Chung, *Philos. Mag.* **1963**, 8, 833.

[55]   G. A. Elbaz, W.-L. Ong, E. A. Doud, P. Kim, D. W. Paley, X. Roy, and J. A. Malen, *Nano Lett.* **2017**, 17, 5734.

[56]   G. A. Slack, D. W. Oliver, G. D. Brower, and J. D. Young, *J. Phys. Chem. Solids* **1977**, 38, 45.

[57]   S. K. Watson, D. G. Cahill, and R. O. Pohl, *Phys. Rev. B* **1989**, 40, 6381.

[58]   W.-L. Ong, E. S. O'Brien, P. S. M. Dougherty, D. W. Paley, C. Fred Higgs III, A. J. H. McGaughey, J. A. Malen, and X. Roy, *Nat. Mater.* **2016**, 16, 83.

[59]   A. A. Kolomenskii, M. Szabadi, and P. Hess, *Appl. Surf. Sci.* **1995**, 86, 591.

[60]   N. H. Tea, R. C. Yu, M. B. Salamon, D. C. Lorents, R. Malhotra, and R. S. Ruoff, *App. Phys. A* **1993**, 56, 219.

[61]   R. Vassen, X. Cao, F. Tietz, D. Basu, and D. Stover, *J. Am. Ceram. Soc.* **2000**, 83, 2023.

[62]   W. Jifang, E. S. Fisher, and M. H. Manghnzmi, *Chin. Phys. Lett.* **1991**, 8, 153.

[63]   F. Thevenot, *J. Eur. Ceram. Soc.* **1990**, 6, 205.

[64]   M. Beekman and D. G. Cahill, *Cryst. Res. and Technol.* **2017**, 52, 1700114.

[65]   Z. Fan, H. Wang, Y. Wu, X. Liu, and Z. Lu, *RSC Adv.* **2016**, 6, 52164.

[66]   Y. Zhang, T. T. Zuo, Z. Tang, M. C. Gao, K. A. Dahmen, P. K. Liaw, and Z. P. Lu, *Prog. Mater. Sci.* **2014**, 61, 1.

[67]   H.-P. Chou, Y.-S. Chang, S.-K. Chen, and J.-W. Yeh, *Mater. Sci. Eng. B* **2009**, 163, 184.

[68]   C. M. Rost, *Entropy-Stabilized Oxides: Explorations of a Novel Class of Multicomponent Materials*, Ph.D. thesis, North Carolina State University, **2016**.

[69]   I. Suzuki, *J. Phys. Earth* **1975**, 23, 145.

[70]   J.E. Keem and J.M. Honig, "Selected Electrical and Thermal Properties of Undoped Nickel Oxide", CINDAS Report 52, West Lafayette, IN, USA **1978.**

[71]   P. Shukla, T. Watanabe, J. C. Nino, J. S. Tulenko, and S. R. Phillpot, *J. Nucl. Mater.* **2008**, 380, 1.

[72]   Z. Rak, C. M. Rost, M. Lim, P. Sarker, C. Toher, S. Curtarolo, J. P. Maria, and D. W. Brenner, *J. of Appl. Phys.* **2016** 120, 095105.

[73]   A. Zunger, S. H. Wei, L. G. Ferreira, and J. E. Bernard, *Phys. Rev. Lett.* **1990**, 65, 353.

[74]   S. Plimpton, *J. Comput. Phys.* **1995**, 117, 1.

[75]   M. S. Green, *J. Chem. Phys.* **1954**, 22, 398.

[76]   R. Kubo, *J. Phys. Soc. Jpn.* **1957**, 12, 570.

[77]   J. W. Lawson, M. S. Daw, and C. W. Bauschlicher, *J. App. Phys.* **2011**, 110, 083507.

[78]   A. Giri, J. L. Braun, C. Rost-Barber, and P. E. Hopkins, *Scr. Mater.* **2017**, 138, 134.

[79]   A. Giri, J. L. Braun, and P. E. Hopkins, *J. App. Phys.* **2018**, 123, 015106.

[80]   M. L. Falk and J. S. Langer, *Phys. Rev. E* **1998**, 57, 7192.

[81]   F. Shimizu, S. Ogata, and J. Li, *Mater. Trans.* **2007**, 48, 2923.